Experiments on the elliptic instability in vortex pairs with axial core flow

CLÉMENT ROY[1,2], THOMAS LEWEKE[1]†, MARK C. THOMPSON[2] AND KERRY HOURIGAN[2,3]

[1]Institut de Recherche sur les Phénomènes Hors Équilibre (IRPHÉ),
CNRS/Universités Aix-Marseille/École Centrale Marseille, 49 rue Frédéric Joliot-Curie, B.P. 146,
F-13384 Marseille CEDEX 13, France

[2]Fluids Laboratory for Aeronautical and Industrial Research (FLAIR), Department of Mechanical
and Aerospace Engineering, Monash University, Melbourne, Victoria 3800, Australia

[3]Division of Biological Engineering, Monash University, Melbourne, Victoria 3800, Australia

Results are presented from an experimental study on the dynamics of pairs of vortices, in which the axial velocity within each core differs from that of the surrounding fluid. Co- and counter-rotating vortex pairs at moderate Reynolds numbers were generated in a water channel from the tips of two rectangular wings. Measurement of the three-dimensional velocity field was accomplished using stereoscopic particle image velocimetry, revealing significant axial velocity deficits in the cores. For counter-rotating pairs, the long-wavelength Crow instability, involving symmetric wavy displacements of the vortices, could be clearly observed using dye visualisation. Measurements of both the axial wavelength and the growth rate of the unstable perturbation field were found to be in good agreement with theoretical predictions based on the full experimentally measured velocity profile of the vortices, including the axial flow. The dye visualisations further revealed the existence of a short-wavelength core instability. Proper orthogonal decomposition of the time series of images from high-speed video recordings allowed a precise characterisation of the instability mode, which involves an interaction of waves with azimuthal wavenumbers $m = 2$ and $m = 0$. This combination of waves fulfils the resonance condition for the elliptic instability mechanism acting in strained vortical flows. A numerical three-dimensional stability analysis of the experimental vortex pair revealed the same unstable mode, and a comparison of the wavelength and growth rate with the values obtained experimentally from dye visualisations shows good agreement. Pairs of co-rotating vortices evolve in the form of a double helix in the water channel. For flow configurations that do not lead to merging of the two vortices over the length of the test section, the same type of short-wave perturbations were observed. As for the counter-rotating case, quantitative measurements of the wavelength and growth rate, and comparison with previous theoretical predictions, again identify the instability as due to the elliptic mechanism. Importantly, the spatial character of the short-wave instability for vortex pairs with axial flow is different from that previously found in pairs without axial flow, which exhibit an azimuthal variation with wavenumber $m = 1$.

Key words: vortex dynamics, vortex instability, vortex interactions

† Email address for correspondence: thomas.leweke@irphe.univ-mrs.fr

1. Introduction

The dynamics and stability of vortex pairs have been the subject of a large number of studies over the last three decades. The development of new experimental techniques and increasing computer capabilities for numerical studies have allowed investigation of these flows to gain a new impetus. The continued interest in this flow is, to a great extent, due to its relevance to the problem of aircraft trailing wakes, whose far-field is primarily composed of a counter-rotating vortex pair. For large modern aircraft, these vortices can attain a considerable strength and represent a significant danger to following aircraft, especially smaller ones, due to the rolling moment and downwash they induce. Therefore, a clear need exists to reduce this effect by accelerating the decay of the wake. One approach is to try to take advantage of the natural 'cooperative' instabilities that can occur in a vortex system. Numerous international projects, listed for example by Gerz, Holzäpfel & Darracq (2002), were developed to investigate the problem. Apart from this very practical motivation, the vortex pair also represents one of the simplest flow configurations for the detailed study of elementary vortex interactions, which may yield useful information for the understanding of the dynamics of more complex transitional or turbulent flows.

The first cooperative instability of a vortex pair to be discovered was a long-wavelength wavy instability that occurs for counter-rotating pairs: the so-called Crow instability. It can be observed in the sky behind aircraft flying at high altitude, when the wake vortices are visualised by condensation (see e.g. the photographs shown in Scorer & Davenport 1970; Tombach 1973; Jacob 1995). Furthermore, some laboratory observations can be found in Sarpkaya (1983), Liu (1992) and Thomas & Auerbach (1994). The first theoretical analysis of this phenomenon was made by Crow (1970). He showed that the mutual interaction of the two vortices can lead to an amplification of displacement perturbations, whose axial wavelength is typically several times the initial vortex separation distance. The sinusoidal vortex displacements are symmetric with respect to the mid-plane between the two vortices, and they lie in planes inclined approximately at $45°$ with respect to the line joining the vortices. The origin of this instability is linked to the balance between the stabilising effect of self-induced rotation of the perturbations and the destabilising influence of the strain field that each vortex induces at the location of its neighbour. It was shown by Kelvin (1880) that a sinusoidal perturbation of a single vortex filament does not grow in time, but rotates around the vortex. In the presence of a second vortex, it can happen that the circumferential component of the velocity field induced by this vortex at the location of the first perturbed filament exactly cancels the self-induced rotation of the latter. The perturbation then remains in a stationary plane and is 'pulled apart' by the radial component of the strain (which is also induced by the second vortex), leading to an exponential growth of its amplitude. A good description of this mechanism and its relation to Kelvin waves can be found in Widnall, Bliss & Tsai (1974).

Many subsequent studies, mostly theoretical and numerical, have illustrated and extended the work of Crow (1970). In particular, the effects of axial flow and arbitrary (axisymmetric) vorticity distributions within the vortices on the stability characteristics were analysed by Widnall, Bliss & Zalay (1971), Moore & Saffman (1973) and Klein, Majda & Damodaran (1995). Extensions of Crow's analysis towards systems of more than two vortices, representative of the near or extended near-wake behind a transport aircraft (possibly with various flap configurations), have also been carried out. The volume of papers in Crouch & Jacquin (2005), which follows the reviews by Spalart (1998), Rossow (1999) and Gerz *et al.* (2002), comprises several of these studies. Although numerical simulations (Rennich & Lele 1997) seem to

confirm the validity of Crow's theory quite closely for the initial evolution of the instability, precise comparison with experimental results is very scarce. Leweke & Williamson (2011) have shown a first detailed comparison with measurements made on vortex pairs without axial flow, showing good agreement. Quantitative results from other experimental studies (Sarpkaya 1983; Thomas & Auerbach 1994; Devenport, Zsoldos & Vogel 1997), as well as observations from full-scale flight tests (Scorer & Davenport 1970), mostly show coarse or only qualitative agreement with theoretical predictions. In this paper, we compare Crow's inviscid theory with experimental results, concerning the wavelength and the growth rate of the long-wave instability in a pair of counter-rotating vortices with axial flow.

The short-wave instability, associated with an elliptic instability (Kerswell 2002), is another cooperative instability that can be observed on a vortex subject to the influence of another vortex. Unlike the Crow instability, whose wavelength is about eight times the vortex separation distance (Crow 1970), the typical wavelength of this instability scales with the radius of the vortex. It is called an 'elliptic instability', since it develops in flows with elliptic streamlines, as found in the core of a vortex subjected to the strain induced by another nearby vortex. This instability can occur in counter-rotating as well as co-rotating configurations, as opposed to the Crow instability, which is inhibited by the rotation of the strain (Jimenez 1975). Since the theory of Crow (1970) is based on the hypothesis of vortex filaments, meaning that the vortices are considered as lines, Crow's work can only apply to a long-wavelength instability. The theoretical basis of a short-wavelength instability such as the elliptic instability has to be explained using different considerations. This was done by Moore & Saffman (1975), who analysed linearly the stability of a finite-core vortex (with a small axial flow), deformed elliptically by the presence of a strain field, in an attempt to explain the unstable vortex rings visualised by Widnall & Sullivan (1973). The same analysis was carried out by Tsai & Widnall (1976). They confirmed Widnall's proposed mechanism (Widnall *et al.* 1974) and concluded that the strain could resonate with two (neutral) Kelvin modes of the vortex, and lead to the exponential growth of a perturbation, thus revealing the mechanism behind the elliptic instability.

A decade later, the numerical simulations of Pierrehumbert (1986) and the Floquet analysis of Bayly (1986) renewed the focus on the elliptic instability. They showed that a two-dimensional inviscid flow with elliptical streamlines is unstable with respect to three-dimensional perturbations in the short-wavelength limit. Landman & Saffman (1987) extended these results to viscous flows, arguing that the presence of viscosity imposes a minimum wavelength for the unstable perturbation. Waleffe (1990) linked the inertial wave approach to the Kelvin mode approach. He analysed the stability of a rotating flow in an elliptical container and showed that a combination of plane waves can lead to localised disturbances whose growth rates match those given by the unbounded theory.

An overall picture of the elliptical instability was given in the review of Kerswell (2002), which concentrated on analytical and numerical results. Perhaps surprisingly, before the results of Leweke & Williamson (1998), who studied the elliptic instability in a pair of counter-rotating vortices, very few quantitative comparisons between predictions and experimental results had been performed. For vortex rings, clear short-wave instability visualisations were originally presented by Krutzsch (1939). They showed that the centreline of the vortex is displaced in the direction opposite to the direction of displacement of peripheral streamlines. This is typical of the elliptic instability in a pair of vortices without axial flow. A short-wave instability was

also observed by Maxworthy (1972) and Widnall & Sullivan (1973). Malkus (1989) explored the nonlinear aspects of the instability in a flow bounded by an elliptical rotating cylinder. Using the same set-up, Eloy, Le Gal & Le Dizès (2000) confirmed some elements of the theory presented by Waleffe (1990). Lacaze, Le Gal & Le Dizès (2004, 2005) extended these results to the flow inside an elliptically deformed rotating sphere.

Thomas & Auerbach (1994) generated two parallel asymmetric vortices by rotating a sharp-edged plate in a water tank. On top of the long-wave instability described by Crow (1970), they were able to visualise a short-wave instability, although the theoretical prediction of Widnall *et al.* (1974) did not seem to match the experimental results. However, a subsequent more precise study carried out by Leweke & Williamson (1998) on a similar symmetric vortex system led to the unambiguous conclusion that the experimental wavelength and growth rate of the short-wave instability did agree well with the theoretical predictions of Tsai & Widnall (1976) and Waleffe (1990). This work was extended by Meunier & Leweke (2001, 2005) to co-rotating vortices. The numerical work of Billant, Brancher & Chomaz (1999) and Laporte & Corjon (2000) confirmed the conclusions of Leweke & Williamson (1998). Up to this point, the theoretical predictions had concerned uniform elliptical vortices (Waleffe 1990). To extend the results to more realistic configurations, Le Dizès & Laporte (2002) obtained an expression for the growth rate of the elliptic instability in a pair of co- and counter-rotating Gaussian vortices that depend on global parameters of the flow. They validated their results by direct numerical simulations (DNS) and large-eddy simulations (LES). They identified unstable bands corresponding to different axial wavenumber ranges. Each band is due to the resonance of the strain field (induced by the other vortex) with two Kelvin modes for which the azimuthal wavenumber m and the frequency ω are $m = \pm 1$ and $\omega = 0$. (Note that although the term 'Kelvin modes' (Kelvin 1880) strictly applies to inviscid normal modes associated with the rotation of the fluid in a stable vortex, we also apply it to the viscous case, as is frequently done in the literature). This is in agreement with the experimental investigations of Leweke & Williamson (1998) and Meunier & Leweke (2001), and the numerical work of Sipp & Jacquin (2003). Some studies (see e.g. Fabre 2002; Fabre & Jacquin 2004) have characterised the short-wave instability on vortices with vorticity distributions more representative of aircraft wakes.

All previous studies were performed on vortices without axial flow, except the early study of Moore & Saffman (1975). The first step to fill this gap was taken by Fabre, Cossu & Jacquin (2000), who discussed the convective and absolute nature of the instability on a pair of Rankine vortices in a uniform axial flow field, subjected to a weak strain. Lacaze, Birbaud & Le Dizès (2005) analysed the stability of a Rankine vortex with an axial velocity core in a stationary strain. They discovered that, contrary to the case without axial flow, Kelvin mode combinations including modes with higher azimuthal symmetry orders and non-zero frequencies could resonate, leading to the instability of the system. The same conclusions were drawn for a Gaussian vortex by Lacaze, Ryan & Le Dizès (2007). For parallel vortices, this corresponds to the counter-rotating case. Recently, these results were numerically extended to the co-rotating case by Roy *et al.* (2008).

Experimental studies of the elliptic instability in a vortex with axial flow have been rare to date. Some visualisations of a short-wave phenomenon in the wake of an aircraft can be found in Scorer & Davenport (1970), Jacob (1995) and Bristol *et al.* (2004). Similar observations were reported by Chen, Jacob & Savaş (1999) and Ortega, Bristol & Savaş (2003), who studied a four-vortex system generated by a
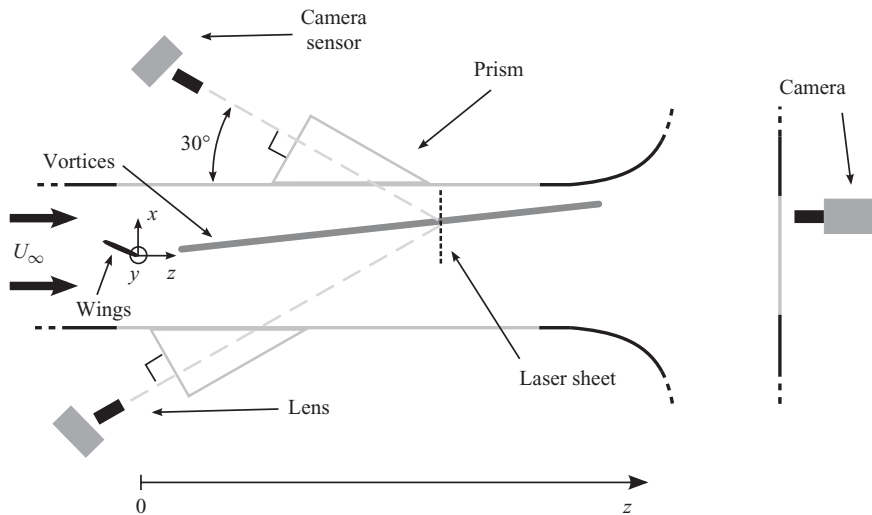
FIGURE 1. Top view of the water channel test section showing the stereo-PIV set-up in a counter-rotating configuration. The tilt angle between the camera sensor and the lens is exaggerated to point out the use of a Scheimpflug mount.

flapped wing in a towing tank. The only known quantitative data were presented by Devenport *et al.* (1997) and Devenport, Vogel & Zsoldos (1999). They investigated counter- and co-rotating vortices generated by two symmetrical wings in a wind tunnel. Some peaks in the velocity spectra measured by hot-wire anemometry seem to be related to the elliptic instability.

In this paper, results are presented concerning experimental co- and counter-rotating vortex pairs with axial flow that very strongly suggest the presence of the elliptic instability. In particular, we analyse the spatio-temporal structure of a short-wavelength perturbation and relate this to the elliptic instability. Specifically, the axial wavelength, the azimuthal wavenumber and the growth rate of the unstable mode are obtained experimentally for a pair of counter-rotating vortices and compared with numerical results. In addition, the spatial characteristics of the unstable mode observed on a co-rotating pair are given and again compared with numerical predictions.

2. Experimental set-up

2.1. *Facility*

The facility used for the experiments is a recirculating water channel with a free surface. The test section has dimensions 37 cm (width) × 50 cm (height) × 150 cm (length). The free-stream velocity U_∞ could be chosen in the range 5–100 cm s^{-1}. The turbulence intensities associated with the streamwise and transverse velocity components are approximately 1.5 % and 0.6 %, respectively. The bottom and sidewalls of the test section are made out of glass. An additional glass window downstream of the test section on the wall normal to the stream allows visual access to the flow inside the test section from five different directions. A schematic diagram is shown in figure 1.

2.2. *Vortex-generating wings*

Two NACA0012 rectangular half-wings made of polyvinyl chloride, each with a chord of $c = 10$ cm, were placed tip-to-tip in the free stream of the water channel. They
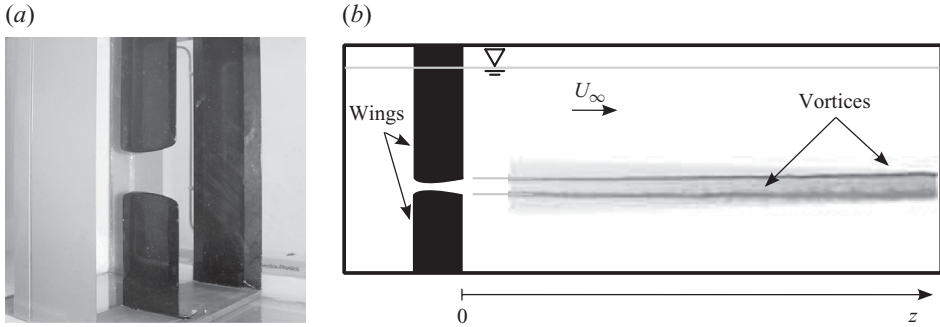
(*a*)   (*b*)

FIGURE 2. (*a*) A photograph of the two half-wings in the water channel. (*b*) Side view of the water channel test section, showing the wings and the resulting vortices in a counter-rotating configuration.

had a round tip with a varying tip diameter equal to the local thickness of the wing. The wings were mounted vertically at the upstream end of the test section. The first half-wing, with a 15 cm span, was fixed on a U-frame positioned along the side and bottom boundaries of the channel. It was possible to change the angle of attack of both wings. The second wing was fixed to a support outside the water, and traversed the free surface. The set-up is illustrated in figure 2(*a*). A similar set-up was used by Devenport *et al.* (1997, 1999).

When a rectangular wing is placed in a uniform stream, a 'wing-tip' vortex is generated (see e.g. Devenport *et al.* 1996). The sign of the circulation of each tip vortex depends on the sign of the angle of attack of the wing. With one vortex being generated by each wing, it is possible to generate a counter- or co-rotating vortex pair by independently adjusting the angle of attack of each wing. Another advantage of this set-up, compared with a flapped wing for instance, is the possibility to translate the top wing along its span direction. The spanwise position of the vortex is close to the wing-tip and mostly depends on the wing-tip shape (Hoerner 1965). Therefore, translating the top wing causes a change in the separation distance b between the two vortices. The three degrees of freedom of this set-up were widely utilised in the exploration phase of the study, the aim being to find an unstable flow clearly exhibiting the elliptic instability. The origin O of the frame-of-reference $\{O, x, y, z\}$ chosen for our study is the middle point of the line linking the wing tips. The z-axis points in the free-stream direction and the y-axis is parallel to the vertical direction, pointing up. The orthogonal frame is completed with the x-axis pointing in the horizontal transverse direction.

2.3. *Flow visualisation*

A dye injection system allowed the visualisation of the vortices. A small pipe network was machined inside the U-frame and the wings to allow injection of fluorescent dye, an aqueous solution of fluorescein. The injection holes were located close to the wing-tip. Different holes were available; depending on the configuration of the wings, the most appropriate holes were selected. The injection was achieved by a pressure difference. Special care was taken to ensure that this had a minimal effect on the developing flow.

The dye injected into the flow was illuminated in volume by an argon ion laser (model Stabilite 2017 from Spectra Physics), coupled to an optical fibre with a spherical lens. The laser was oriented in the axis of the vortices through the

downstream visualisation window presented in figure 1. Side view photographs of the vortices were taken with a camera (Nikon D200) looking through the sidewalls of the channel test section. When a high acquisition frame rate was needed, a monochrome high-speed video camera (Vision Research Phantom V5) was used. Some visualisations of the vortices were taken in a plane normal to the free stream. In that case, the optical fibre was coupled to a cylindrical lens, allowing the resulting laser sheet to be oriented from bottom to top. The D200 still camera or the Phantom camera was then positioned to take images through the downstream visualisation window.

2.4. *Velocity measurements*

All velocity measurements were made using stereoscopic particle image velocimetry (stereo-PIV). This technique allows the measurement of three velocity components in a plane. Successful implementation of this method has been presented in e.g. Willert (1997), Alkislar, Krothapali & Lourenco (2003) and Carlier & Stanislas (2005). An Nd-YAG pulsed laser was positioned underneath the test section at the desired distance from the wing, generating a 3 mm thick vertical light sheet (see figure 1). The flow was seeded with silver-coated particles (Dantec), whose size (100 μm diameter) was small compared with the characteristic scale of the vortex (diameter typically of the order of 1 cm). Pictures of the particles in the laser sheet were taken with two high-resolution digital cameras (Roper Redlake, 4000×2672 pixels). Each camera was placed on one side of the test section (see figure 1), viewing the laser plane in a direction forming a $30°$ angle with the free stream. The camera sensor and the lens were mounted on a Scheimpflug set-up (Scheimpflug 1904). To conserve the orthogonality between the lines of sight of the cameras and the air–liquid interface, water-filled glass prisms were fixed on the test section sidewalls (see figure 1). This reduces the distortion entailed by the non-orthogonal angle of sight. In addition, the small gaps between the prisms and the channel sidewalls were filled with water to alleviate the reflection of the light at the air–glass interfaces. An overview of the stereo-PIV technique coupled with the use of prisms and Scheimpflug mounts can be found in Prasad & Jensen (1995) and Zang & Prasad (1997). The computing algorithm used to process the images is based on a two-dimensional cross-correlation PIV code developed by Meunier & Leweke (2003), which was successfully used in previous experimental studies on vortex flows (see e.g. Meunier & Leweke 2005; Boulanger, Meunier & Le Dizès 2007, 2008).

2.5. *Parameters of the flow and vortex models*

For a vortex, a Reynolds number can be defined by $Re = \Gamma/\nu$, based on the total circulation. Another important parameter is the non-dimensional core size a/b, where a is the vorticity radius (defined below) and b is the vortex separation distance. The interaction between the vortices as they advect downstream is a strong function of a/b. The axial flow parameter $W_0 = (U_0 - U_\infty)2\pi a/\Gamma$, where U_0 is the axial velocity at the centre of the vortex and U_∞ is the free-stream velocity, compares the axial velocity defect on the vortex axis with a characteristic azimuthal velocity. We also introduce a_w/a, the ratio between the radial scale a_w of the axial velocity profile and the core radius a.

Two different theoretical models were used to try to characterise the vorticity/velocity fields obtained experimentally. The first is the well-known Gaussian

model. This prescribes the axial vorticity, ζ, as

$$\zeta(r) = \frac{\Gamma}{\pi a^2} \exp(-r^2/a^2), \tag{2.1}$$

where r is the distance from the centre of the vortex.

We also use a more recent vortex model called VM2 by Fabre & Jacquin (2004). Following their approach, the azimuthal velocity profile U_θ can be modelled according to

$$U_\theta = \frac{\Gamma}{2\pi} \frac{\rho_2^{\gamma-1}}{\rho_1^{\gamma+1}} \frac{r}{[1 + (r/\rho_1)^4]^{(1+\gamma)/4}[1 + (r/\rho_2)^4]^{(1-\gamma)/4}}, \tag{2.2}$$

where ρ_1 and ρ_2 correspond to two different characteristic radii of the vortex. Here ρ_1 delimits the inner viscous core containing most of the circulation, and ρ_2 defines the extent of the region containing all the circulation. In the region $\rho_1 < r < \rho_2$, the azimuthal velocity varies approximately as $r^{-\gamma}$. For many types of wing-tip vortices, ρ_2 is significantly larger than ρ_1. This model appears particularly useful to describe commonly observed vortices.

3. Counter-rotating vortex pair

In this section, we focus on the three-dimensional instabilities of a pair of counter-rotating vortices. After an exploration of different parameter ranges, one configuration was chosen for a more detailed analysis. The selected configuration provided the clearest visualisations and PIV results. The strength of the trailing vortices increases with angle of attack, so it makes sense to choose the largest angle possible. However, if the angle of attack is too large, the flow separates as it passes over the aerofoil and the downstream flow then becomes unsteady. First, we describe the experimental base flow measured in the water channel with the stereo-PIV technique. After a brief analysis of the long-wavelength Crow instability, we present visualisations of a short-wavelength instability mode of the vortices. In order to make the link between this observation and the elliptic instability theory, we estimate the growth rate, the wavelength and the azimuthal wavenumber of the observed instability mode. Visualisations and proper orthogonal decomposition (POD) techniques are used to extract the spatial structure and the temporal dependence of the instability mode. These data are compared with results of a numerical stability analysis based on the actual experimental base flow.

3.1. *Three-dimensional base flow*

The wings were positioned in the counter-rotating configuration, in the middle of the water channel section. Both angles of attack were equal to $8.5°$. The wing tips were positioned 3 cm apart. The free-stream velocity was approximately equal to $56 \, \mathrm{cm \, s^{-1}}$. Two vortices were generated at the wing tips. The top vortex circulation was positive so that the vortex pair translated in the positive y-direction by mutual induction. In the following, indices 1 and 2 refer to the top and bottom vortices, respectively. Stereo-PIV measurements were performed in two planes normal to the axis of the water channel, located at $z/c = 5.6$ and $z/c = 9.4$. For each plane, 300 three-dimensional velocity fields were obtained using the procedure described in §2.4.

The mean axial vorticity (ζ) and axial velocity (U) distributions at $z/c = 5.6$ are presented in figure 3. The axial velocity field shows a large deficit in the vicinity of the vortices. Residuals of the velocity defects behind the main parts of the wings can also be identified, to the left of the vortex cores. Driven by their respective vortices, the wakes of the two half-wings are advected towards the centre of the vortex pair. The
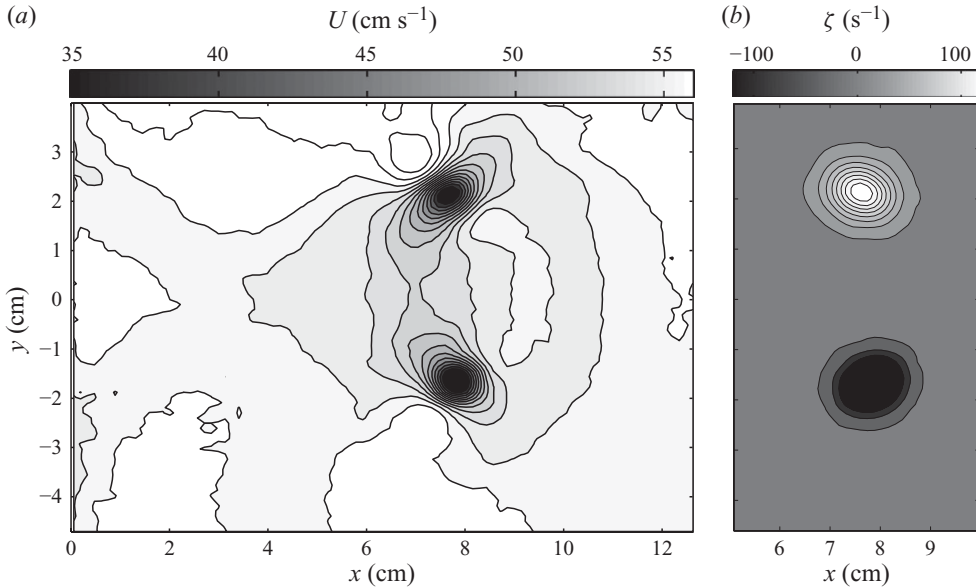
FIGURE 3. (*a*) Average axial velocity U and (*b*) axial vorticity ζ, for $z/c = 5.6$.

axial velocity distribution in the vortex core is therefore strongly non-axisymmetric. This fact is reinforced by the presence of a small axial velocity excess located about 1 cm away from the top vortex, in the top-left direction (see figure 3). A small symmetrical decrease of the axial velocity can be observed close to the bottom vortex, which is difficult to explain. Though the axial velocity fields presented by Devenport *et al.* (1997), who used the same half-wing set-up in a wind-tunnel, did not exhibit any velocity excess, a rapid increase of the axial velocity can be found in approximately the same position relative to the vortex pair.

The distribution of the average axial vorticity in the vortex cores is elongated in a direction approximately normal to the elongation direction of the average axial velocity distribution. Although the latter deformation is, as explained above, mainly due to the residual velocity defect caused by the wing, the elongation of the vorticity distribution is, for the most part, due to the displacement of the vortices in a preferred direction, which explains this difference. To characterise this motion, the location of the vortices was determined for each of the 300 individual fields at $z/c = 5.6$ and $z/c = 9.4$. This was achieved by fitting the measured two-dimensional velocity field with the two-dimensional field of a pair of axisymmetric counter-rotating Gaussian vortices. The free parameters of this fit were, for each vortex, the total circulation, the Gaussian radius and the coordinates of the vortex centres in the (O, x, y) plane. In order to characterise the vortex motion, the eigenvalues a_M^2 and a_m^2 ($a_M > a_m$) of the covariance matrix of the vortex positions were computed. The eigenvector corresponding to a_M^2 is the direction in which the variance of the vortex position projection is maximised. The normal direction minimises the variance a_m^2. Physically, the direction corresponding to the a_M eigenvector is the preferred direction of motion of the vortex. We can illustrate this graphically by an ellipse centred on the average position of the vortex, of major and minor axes a_M and a_m, respectively, oriented according to the respective eigenvectors. The preferred direction of motion is characterised by the angle α formed by the line joining the average positions of

		$z/c = 5.6$		$z/c = 9.4$	
		Top vortex	Bottom vortex	Top vortex	Bottom vortex
α	degree	55.5	59.6	45.1	59.4
a_m	cm	0.08	0.07	0.14	0.16
a_M	cm	0.15	0.17	0.33	0.36
Γ	cm^2 s^{-1}	160	-155	160	-156
a	cm	0.56	0.54	0.60	0.61
b	cm		3.81		4.18
a_w	cm	0.49	0.46	0.56	0.52
Γ/ν		17 000	$-16\,500$	17 000	$-16\,700$
a/b		0.147	0.142	0.143	0.146
a_w/a		0.88	0.85	0.93	0.85
W_0		-0.41	0.43	-0.47	0.49

TABLE 1. Parameters of the base flow extracted from the stereo-PIV measurements.
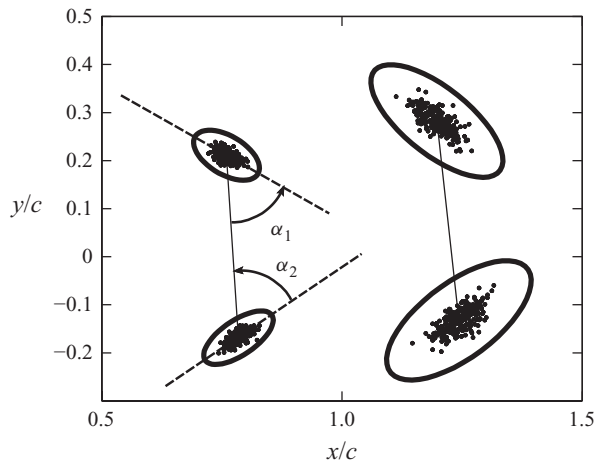
FIGURE 4. Vortex positions for $z/c = 5.6$ (left) and $z/c = 9.4$ (right). Each dot represents one position of the vortex extracted from one velocity field. A solid line links the mean positions of the top and bottom vortices. For each vortex, an ellipse of half-axes a_M and a_m (see table 1), oriented in the preferred direction of motion, is plotted. Note that a_M and a_m are magnified by a factor of 5.

the vortices and the preferred direction of motion of one vortex (see figure 4). For each vortex, the values obtained for α, a_M and a_m are listed in table 1. Two physical mechanisms can explain the increase of a_m and a_M with z. The first can be linked to the dynamics of a single vortex. The same trend was observed by Devenport *et al.* (1996), who used hot-wire anemometry to estimate the amplitude of the lateral motion of a single trailing vortex, the so-called vortex meandering (Roy & Leweke 2008). This phenomenon is currently not fully understood; a probable explanation is related to transient growth of perturbations triggered by random external perturbations (Antkowiak & Brancher 2004; Fontane, Brancher & Fabre 2008; Roy & Leweke 2008), which can either come from the turbulence of the free stream, or be generated in the wake of the wing, possibly through flow separation at the relatively low Reynolds numbers considered here. The development of the Crow instability is the second factor leading to an increase of a_M and a_m, as the amplitude of the long
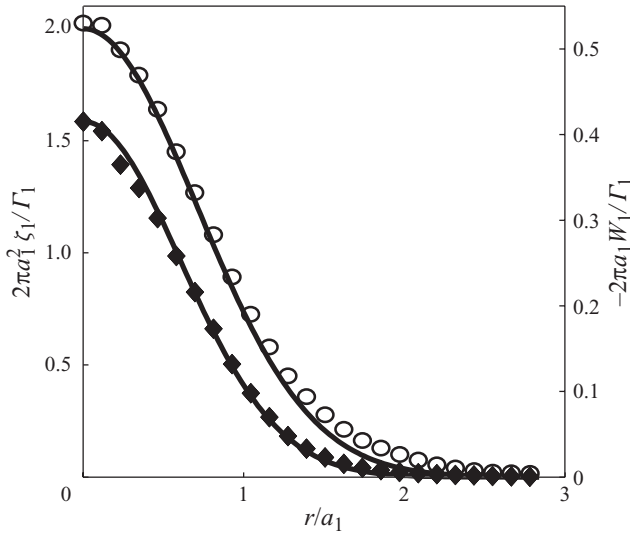
FIGURE 5. Azimuthally averaged vorticity ζ (circles) and axial velocity defect W (diamonds) profiles for the top vortex, at $z/c = 5.6$. The experimental data are fitted with Gaussian functions (solid lines).

sinusoidal deformations of the vortices increases. This aspect of the flow is discussed in §3.2. The mean separation distance b between the vortices increases by 10 % between $z/c = 5.6$ and $z/c = 9.4$. The same trend was observed by Devenport *et al.* (1996).

The transverse displacement of the vortices due to vortex meandering and the Crow instability has an effect on the fields presented in figure 3: the size of the vortex cores are overestimated, especially in the preferred direction of motion, and the axial velocity in the centre of the vortices is underestimated. It is possible to minimise this effect by taking advantage of the knowledge of the vortex positions before averaging the fields. Each field is translated so that the centre of one vortex centre lies in its previously computed mean position, before averaging the fields. The operation is then repeated for the second vortex.

For each vortex, the total circulation Γ was estimated by integrating the velocity on a rectangular contour surrounding the vortex. The contour was chosen as large as possible to take into account as much vorticity as possible. One side of the contour was the centreline separating the two vortices. The values obtained show that the top vortex was stronger than the bottom vortex (see table 1). This difference in circulation entails a rotation of the pair, whose angular velocity can be estimated from the change in orientation of the line joining the two vortex centroids between the two downstream positions. The resulting value of $3.1° \, \mathrm{s}^{-1}$ is in reasonable agreement with the value predicted by a point-vortex model: $(\Gamma_1 + \Gamma_2)/2\pi b^2 = 2.8° \, \mathrm{s}^{-1}$ (using the data in table 1 and a representative 'mean' separation distance $b = 4 \, \mathrm{cm}$). The experimental translation velocity of the pair, $6.4 \, \mathrm{cm \, s}^{-1}$, is also in good agreement with the translation velocity of a point-vortex pair with circulations $\pm\Gamma = 157 \, \mathrm{cm}^2 \, \mathrm{s}^{-1}$ and separation distance $b = 4 \, \mathrm{cm}$: $\Gamma/2\pi b = 6.2 \, \mathrm{cm \, s}^{-1}$.

The vorticity profiles were evaluated by computing the azimuthal average of the mean vorticity field obtained by the recentring method described above. The mean field was then fitted with a Gaussian function defined in (2.1) to extract a vorticity radius a. As shown in figure 5 for the top vortex (index 1), the Gaussian function
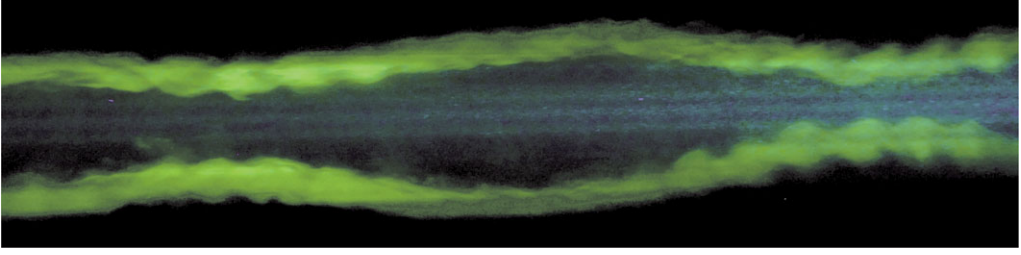
FIGURE 6. (Colour online available at journals.cambridge.org/FLM) Visualisation of the Crow instability of a pair of counter-rotating vortices with axial core flow. The short-wavelength oscillation corresponding to the elliptic instability is also visible. The field of view is approximately 8 cm × 33 cm.

matches the experimental data well. A slight local underestimation of the vorticity is only observed around the radial position $r/a = 1.8$. Since the circulation was imposed during the fit, it imposes only a small error on the spatial distribution of the vorticity but the overall vorticity is correctly represented.

For each vortex, U_∞ is defined as the value of the axial velocity at $r/a = 3$. By subtracting U_∞ from the axisymmetric axial velocity profile, we define the axial velocity defect profile W. Here U_0 is the axial velocity at the centre of the vortex. As with the vorticity, W is fitted to a Gaussian function (see relation (2.1) and figure 5), the axial velocity radius a_w being the only free parameter. The match is excellent. The values of all vortex parameters are listed in table 1. We note an increase of the radius a with downstream distance much faster than suggested by viscous diffusion at this Reynolds number. At $z/c = 9.4$, the flow is highly turbulent, subject to vortex meandering and the Crow instability. Under these conditions, the determination of the vortex centre in individual PIV measurements is subject to errors and uncertainties, which leads to a spurious broadening of the average fields, despite the use of the recentring method.

3.2. *Crow instability*

One major ingredient of the counter-rotating vortex pair flow is a symmetric wavy deformation of the vortices, whose axial wavelength λ_c is several times the vortex separation distance b. This long-wavelength instability was first analysed by Crow (1970), who considered a pair of Rankine vortices with core radius a_e, whose dynamics is governed by Biot–Savart induction. He showed that symmetric sinusoidal deformations of the pair could become unstable under the combined effects of mutual induction and self-induced motion of the vortices. He calculated the non-dimensional growth rate $\sigma_c^* = \sigma_c (2\pi b^2/\Gamma)$, where σ_c is the dimensional rate, as a function of λ_c/b and a_e/b, using a long-wavelength approximation (valid for $a_e/\lambda_c \lesssim 0.06$) for the self-induced rotation rate.

The self-induced dynamics of vortices with arbitrary (axisymmetric) velocity profiles was analysed by Widnall *et al.* (1971), and subsequently by Moore & Saffman (1973), Leibovich, Brown & Patel (1986) and Klein & Knio (1995), in the limit of long wavelengths. It can be deduced from this work that a vortex, with azimuthal and axial velocity distributions $v_\phi(r)$ and $v_z(r)$ evolving on a characteristic radial scale a, exhibits the same self-induced dynamics as an equivalent Rankine vortex, having the same circulation Γ and a core radius

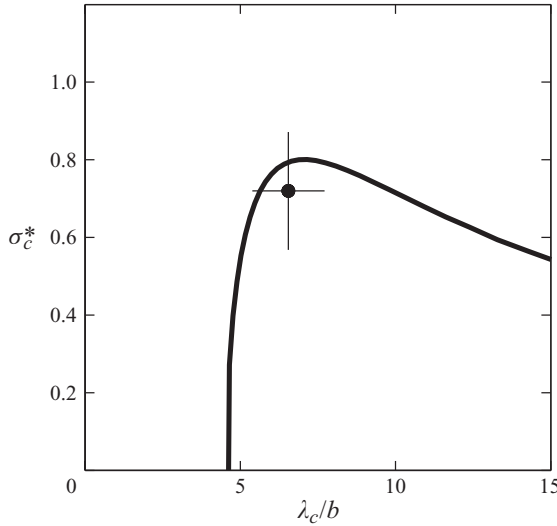$$a_e = a \exp\left[\tfrac{1}{4} - A + C\right], \tag{3.1}$$

FIGURE 7. Growth rate of the Crow instability as a function of wavelength. The solid line is the theoretical growth rate σ_c, according to Crow (1970). The solid circle is the experimental result.

where A and C are integral parameters characterising the velocity profiles; they are given by

$$A = \lim_{r \to \infty} \left[\frac{4\pi^2}{\Gamma^2} \int_0^r \bar{r} v_\phi^2(\bar{r}) \, \mathrm{d}\bar{r} - \ln \frac{r}{a} \right], \tag{3.2}$$

$$C = \frac{8\pi^2}{\Gamma^2} \int_0^\infty \bar{r} v_z^2(\bar{r}) \, \mathrm{d}\bar{r}. \tag{3.3}$$

Using the Gaussian functions to model the vortex profiles, we can theoretically determine A and C by means of (3.2) and (3.3). Numerically, we obtain $A_1 \approx -0.0580$ and $C_1 \approx 0.0639$. Therefore,

$$a_e \approx 1.4575a. \tag{3.4}$$

With the results of Crow (1970), we can then obtain a prediction for the growth rate of the long-wavelength instability in our pair of counter-rotating vortices.

The experimental wavelength λ_c was measured by taking the average of 200 measurements from the set of visualisations obtained at $z/c = 9.2$. We find $\lambda_c/b = 6.55$, with a standard deviation of 0.6. An estimation of the experimental growth rate σ_c can be obtained by comparing the amplitude of a_M for the top vortex, between $z/c = 5.6$ and $z/c = 9.4$, with an estimated uncertainty of $\pm 20\%$. Experimentally, we find

$$\left. \begin{array}{l} \lambda_c/b = 6.55 \pm 0.60 \\ \sigma_c^* = 0.72 \pm 0.14 \end{array} \right\} \text{(experimental).} \tag{3.5}$$

Figure 7 compares the theoretical prediction with the experimental measurement. The theoretical maximum growth rate and the corresponding wavelength, determined from Crow (1970), are

$$\left. \begin{array}{l} \lambda_c/b = 7.07 \\ \sigma_c^* = 0.80 \end{array} \right\} \text{(theoretical).} \tag{3.6}$$

The agreement between the two results is very good.

3.3. *Elliptic instability*

3.3.1. *Theoretical aspects*

The theory of the elliptic instability is based on linear normal modes. Following this formalism, the perturbation velocity field $\boldsymbol{u}'$ and the pressure field p' are written as

$$(\boldsymbol{u}', p') = [\boldsymbol{u}(r), p(r)] \exp(\mathrm{i}kz + \mathrm{i}m\theta - \mathrm{i}\omega t), \tag{3.7}$$

where k and m are the axial and azimuthal wavenumbers and ω is the angular frequency. For the case of a Rankine vortex without axial flow, the linear normal-mode solutions of the relevant dispersion relation, $D(k, m, n) = 0$, are the so-called Kelvin modes. For each azimuthal wavenumber, m, there exists an infinity of branches in the (k, ω) plane that are solutions of the dispersion relation. To classify these branches, the label n is commonly used. It corresponds to the number of zeros of the radial velocity, u_r, in the interval $0 < r < a$. Arendt, Fritts & Andreassen (1997) showed that Kelvin modes form a basis for the perturbations localised in the vortex core. This means that any perturbation in the core of a Rankine vortex can be expressed by a combination of Kelvin modes. Moore & Saffman (1975) and Tsai & Widnall (1976), who were not aware of this property, showed that a resonance of Kelvin modes with the strain leads to (elliptic) instability. They studied a vortex with finite core size immersed in a weak strain field of second-order azimuthal symmetry. They showed that the strain field could resonate with two Kelvin modes of azimuthal wavenumbers $m_1 = 1$ and $m_2 = -1$.

These results can be generalised for higher azimuthal wavenumbers (Eloy & Le Dizès 2001). The general resonance condition coupling the strain with two Kelvin modes with (k_1, m_1, ω_1) and (k_2, m_2, ω_2), reads

$$\begin{pmatrix} k_1 \\ m_1 \\ \omega_1 \end{pmatrix} - \begin{pmatrix} k_2 \\ m_2 \\ \omega_2 \end{pmatrix} = \begin{pmatrix} 0 \\ \pm 2 \\ 0 \end{pmatrix}. \tag{3.8}$$

Two Kelvin waves can therefore resonate with the strain if their axial wavenumber and frequency are equal and their azimuthal wavenumbers differ by 2. Eloy & Le Dizès (2001) showed that, for the case $(m_1, m_2) = (-1, 1)$, the growth rate is maximised when the labels n of the two Kelvin modes are equal. The instability mode is in this case referred to as the *principal* mode and can be identified by the triplet (m_1, m_2, n).

These results were later extended to vortices with continuous vorticity profiles. Le Dizès & Laporte (2002) gave an expression for the growth rate in a pair of Gaussian vortices (co- and counter-rotating) without axial flow. They found that the most unstable modes are necessarily a combination of two Kelvin modes of azimuthal wavenumbers -1 and 1. This is consistent with the experimental results of Leweke & Williamson (1998), who studied the instability in a pair of counter-rotating vortices and observed an unstable periodic displacement of the vortex centres.

Lacaze et al. (2007) studied the instability of a Batchelor vortex in a stationary strain field. As for the counter-rotating case, they found that the triadic resonance of the two Kelvin modes with the strain field was still leading to instability. Interestingly, they showed that when the axial velocity amplitude increases, the $(-1, 1)$ modes become damped. There exists a value of the axial flow parameter, W_0, above which the $(-1, 1)$ modes are no longer the most unstable. Instead, modes with a more complex spatial structure, such as $(-2, 0)$, can be observed.
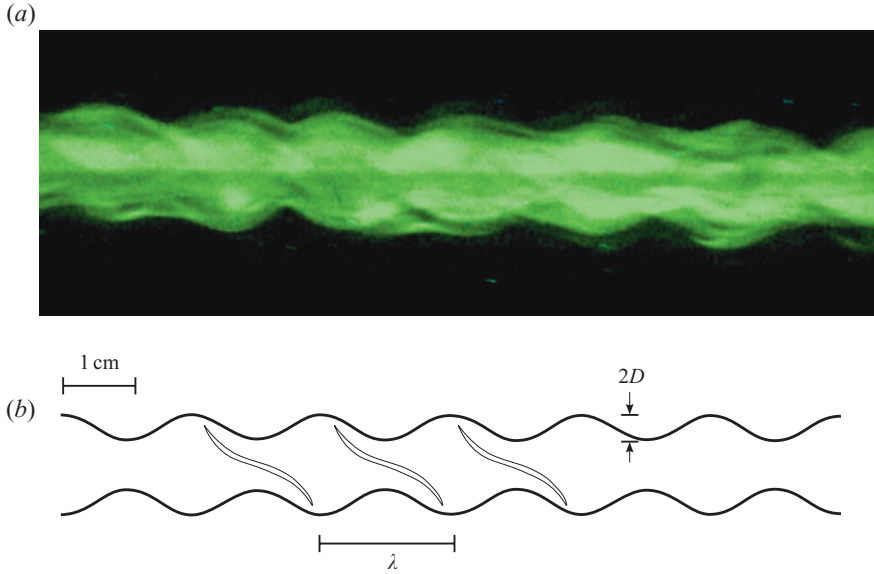
(*a*)

(*b*)

FIGURE 8. (Colour online) (*a*) Visualisation of the elliptic instability on the top vortex of figure 6. (*b*) Schematic diagram showing the characteristic scales.

3.3.2. *Experimental observations*

It can be seen in figure 6 that a short-wavelength core deformation is present on top of the Crow instability. We analyse here in detail this perturbation, focusing on the upper trailing vortex of figure 6.

To observe the perturbation more closely, the laser beam was oriented in the upstream direction through the visualisation window (see figure 1). Fluorescein dye was injected into the top vortex and illuminated by the laser beam, and a camera was placed on the side of the test section, aiming at the vortex in the y-direction. Figure 8(*a*) shows a periodic perturbation propagating on the top vortex. It is symmetric with respect to the axis of the vortex in this view. The well-organised structure that can be seen in figure 8(*a*) was not observable on all frames. Only 80 frames (of 300 taken) could be analysed for $z/c = 9.0$ to extract a wavelength λ_1. Averaging the measured wavelengths, we obtain $\lambda_1 = 1.60$ cm with a standard deviation of 0.15 cm. The non-dimensional axial wavenumber is $k_1 a_1 = 2.21 \pm 0.14$.

In order to estimate the growth rate of these short-wavelength oscillations, measurements of the amplitude D of the perturbation, defined in figure 8(*b*), were performed at $z/c = 7.2$, 7.8, 8.4, 9.0 and 9.7 on the top vortex. At each streamwise position, 200 frames were recorded; 20 of them, showing the instability clearly, were selected and processed. The growth rate σ_1 is then estimated by a linear regression, taking into account the 100 amplitudes measured (see figure 9). We find

$$\sigma_1^* = \sigma_1 \frac{2\pi b^2}{\Gamma_1} = 0.90 \pm 0.09, \qquad (3.9)$$

with b and Γ_1 taking the values measured at $z/c = 5.6$ (see table 1). The uncertainty of the measurements of the amplitude D is high; typically, the standard deviation reaches 30 % of the mean value. This is due to the fact that the Crow instability is fully developed at this downstream location, generating a high variance of the separation distance b. Nevertheless, the resulting uncertainty of the growth rate σ_1 is
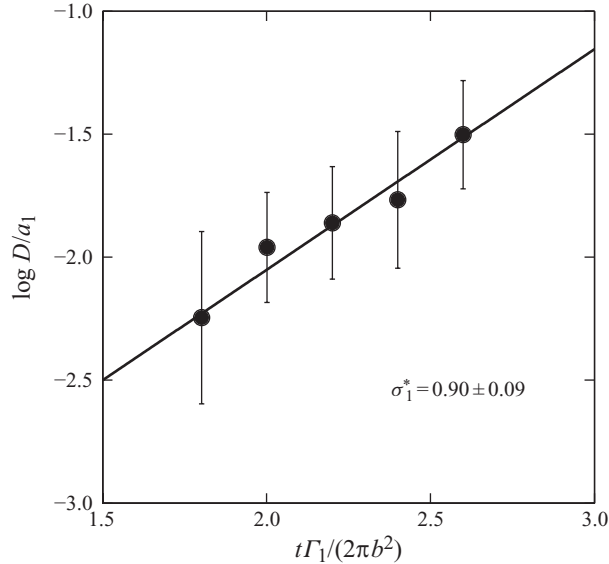
FIGURE 9. Amplitude of the oscillations measured for different streamwise positions. The solid circles represent the experimental data. The linear regression symbolised by the solid line leads to the growth rate prediction σ_1.

only 7 %. (The evaluation of the uncertainty in the computation of σ_1^* results directly from the least-squares analysis. It is described e.g. by Taylor 1997.)

In order to link these experimental results to a known instability mechanism, a linear stability analysis was performed numerically using the full spectral code presented in Roy *et al.* (2008). The base flow investigated was chosen to be very similar to the flow measured at $z/c = 5.6$. At this location, the roll-up phase of the vorticity sheet is terminated and the amplitudes of the Crow instability and of vortex meandering are still reasonably small. The short-wavelength perturbation is not visible as close to the wings. However, the wavelength selection is expected to occur in this region. The base flow to be analysed was generated by solving the two-dimensional Navier–Stokes equations, starting from two axisymmetric vortices with Gaussian vorticity profiles and circulation Γ. After a short period of oscillation during which the vortices relax to adapt to their mutually induced strain, a quasi-steady mean state is reached (Le Dizès & Verga 2002). The flow obtained is a quasi-steady solution of the Euler equations. It is then possible to stop the diffusion process and perform a stability analysis of the flow with respect to three-dimensional perturbations. The vorticity radius a of the flow is measured by fitting the velocity field with the two-dimensional velocity field of a pair of axisymmetric vortices. The axial velocity is then imposed artificially according to

$$U_c(\theta, r) = W_0 \frac{\Gamma}{2\pi a} \left[\frac{\xi_c(\theta, r)}{\xi_c(0, 0)} \right]^{a^2/a_w^2}, \qquad (3.10)$$

where $U_c(\theta, r)$ and $\xi_c(\theta, r)$ are the two-dimensional fields of axial velocity and axial vorticity in the cylindrical frame centred on each vortex. The parameters of the numerical base flow are presented in table 2. The numerical growth rate is plotted in figure 10(a) as a function of the axial wavenumber. The most unstable zone, located around $k_1 a_1 = 1.75$, corresponds to the elliptic instability. It was identified

	Experiment	Simulation
a_1/b	0.147	0.147
a_2/b	0.142	0.147
a_{w1}/a_1	0.88	0.88
a_{w2}/a_2	0.85	0.88
Γ_1/ν	17 000	16 800
Γ_2/ν	$-16\,500$	$-16\,800$
W_{01}	-0.41	-0.41
W_{02}	0.43	0.41
$\sigma\,2\pi b^2/\Gamma$	0.90	0.96
$k_m a$	2.21	1.75

TABLE 2. Parameters of the experimental (at $z/c = 5.6$) and numerical flows for counter-rotating vortices.
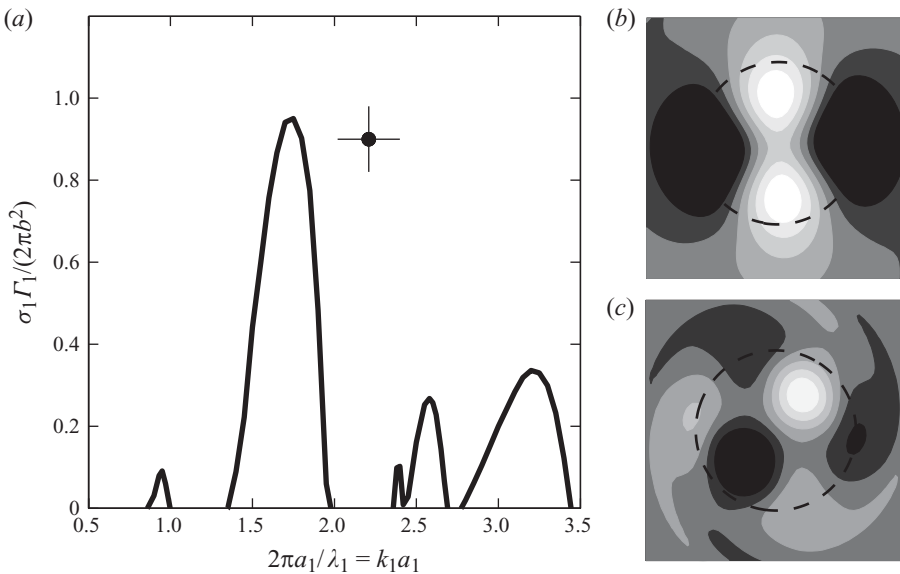
FIGURE 10. (*a*) Non-dimensional growth rate as a function of the axial wavenumber. The solid line represents the numerical result. The dot symbolises the experimental point. The mode structures corresponding to $k_1a_1 = 1.75$ and 3.2 are presented in (*b*) and (*c*).

as the mode $(0, 2, 1)$ (see § 3.3.1). The spatial structure of this mode is presented in figure 10(*b*). This unstable mode was theoretically predicted by Lacaze *et al.* (2007) for a pair of counter-rotating Gaussian vortices. The second-order azimuthal symmetry of this mode is coherent with the structure of the experimental perturbation observed, which is symmetric with respect to the vortex axis. The second most unstable zone, around $k_1a_1 = 3.2$, has an azimuthal symmetry of first and third orders, as shown in figure 10(*c*), and is therefore not a candidate to match the visualisations. The difference between the non-dimensional wavenumber k_m corresponding to the largest growth rate and the experimental wavenumber k_1a_1 is about 20 %. This discrepancy is most likely due to the uncertainty in identifying the base flow responsible for the wavelength selection. Indeed, the wavelength of the instability is determined by the conditions corresponding to the early stages of the flow. This means that the location $z/c = 5.6$, at which the base flow was measured, may already be too far downstream
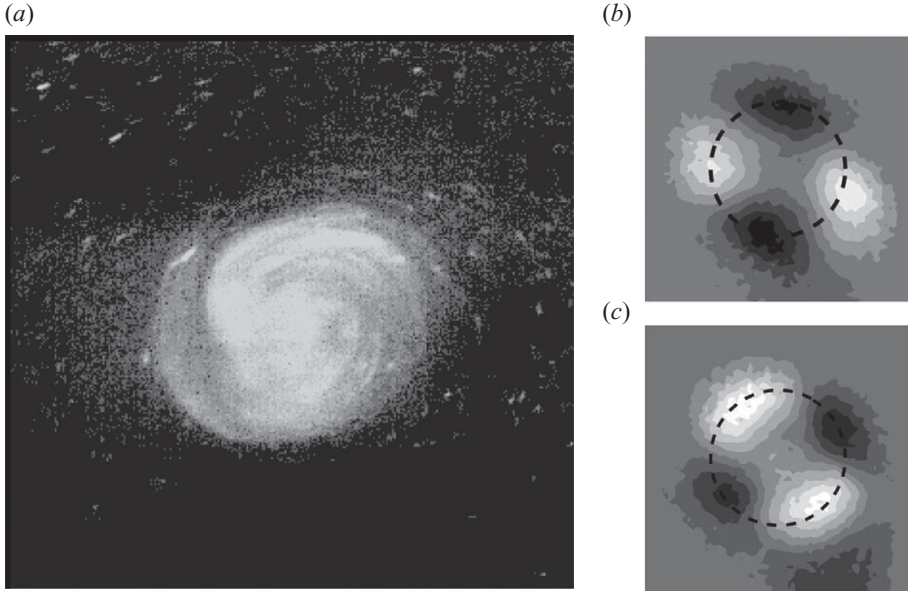
(a)

(b)

(c)

FIGURE 11. (*a*) Example of a visualisation used to perform the POD analysis on the light intensity. (*b*) Mode 5 and (*c*) mode 6 of the POD analysis. The dotted line is a circle of radius a_1.

of the wing. A more upstream position would yield a smaller vorticity radius a_1 (the radius between $z/c = 5.6$ and $z/c = 9.4$ increased by 7 %). Also, considering the mode $(0, -2, 1)$ for $W_0 > 0$, k_m increases with $|W_0|$, as shown by Lacaze *et al.* (2007) and Roy *et al.* (2008). Underestimating U_∞ would therefore lower the wavenumber. Despite this, the values of the experimental and numerical growth rates match well, given the experimental uncertainty.

Further details of the spatial structure of the instability were obtained from a different set of visualisations, with a laser sheet oriented vertically, normal to the free stream. Images of the top vortex were taken through the visualisation window presented in figure 1, in a direction normal to the laser sheet; figure 11(*a*) shows an example. The Phantom high-speed camera was used to acquire 4000 frames at a rate of 300 Hz. The next step involved the so-called proper orthogonal decomposition of this visualisation image series. Reviews of the POD method can be found in Berkooz, Holmes & Lumley (1993) and Liang *et al.* (2002). A didactic approach is shown in Chatterjee (2000). In a previous study on the dynamics of a single wing-tip vortex, it was shown that, concerning the qualitative spatial structure, a POD of a series of dye images gave results effectively identical to those of a POD of vorticity fields (Roy & Leweke 2008, see also the Appendix below). In the present study, the dye POD was used for its ease of implementation, in order to extract the main features of the short-wave instability.

The method used for our decomposition can be explained as follows: the 8000 pixels of each frame centred on the top vortex were aligned to form one column of a matrix $\boldsymbol{F}$. A singular value decomposition of $\boldsymbol{F}$, which is of the form

$$\boldsymbol{F} = \tilde{\boldsymbol{U}} \boldsymbol{\Sigma} \tilde{\boldsymbol{V}}, \tag{3.11}$$

was then performed. In equation (3.11), the diagonal elements S of $\boldsymbol{\Sigma}$ are the singular values of $\boldsymbol{F}$, arranged in decreasing order. All other elements of $\boldsymbol{\Sigma}$ are zero. The
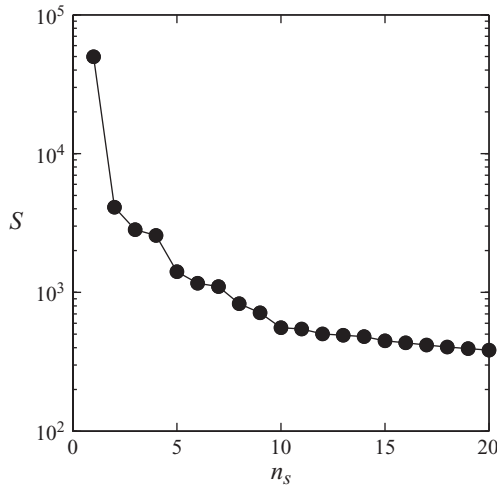
FIGURE 12. Singular values S computed from the light intensity of 4000 pictures of the top vortex.
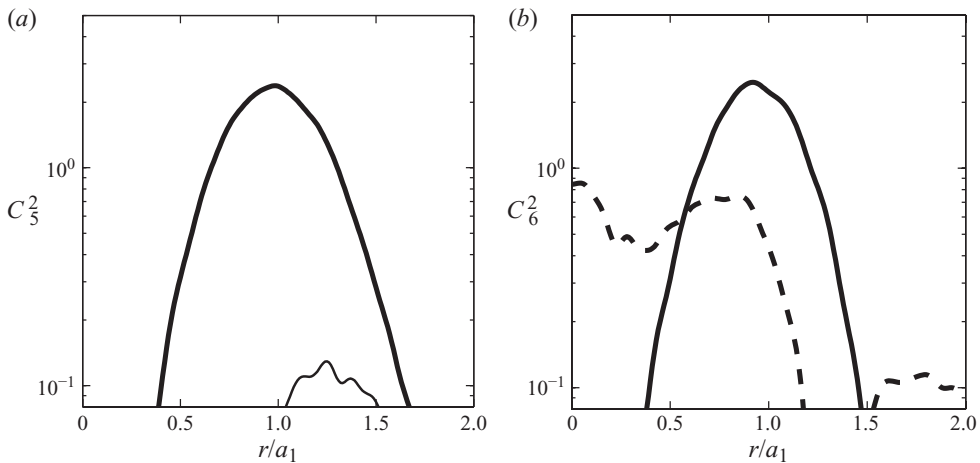

FIGURE 13. The squares of the Fourier coefficients (*a*) C_5 and (*b*) C_6 are plotted for modes 5 and 6, as a function of r. The thick, thin and dashed lines correspond to $m = 2$, $m = 3$ and $m = 0$ respectively. The other branches for which $m < 10$ are too weak to appear on the figures.

columns of $\tilde{U}$ are the corresponding singular vectors. They are orthonormal and form a basis for the original frames. This basis is optimal in the least-squares sense. For any integer $n_i \leqslant 4000$, it is not possible to find a basis for which the approximation of the frame series is better than the approximation with the first n_i singular vectors. We call n_s the rank of a singular value in the decreasing hierarchy. The first singular values of F are presented in figure 12, showing, as expected, a decrease of the variance (or energy) of the modes with increasing rank. Since the POD was performed on the light intensity values, the units of the singular values, such as those of the Fourier coefficients and the power spectral densities presented in figures 13 and 15, are not physically relevant.

POD allows the sequence of time-varying fields, in this case light intensity images, to be decomposed into its dominant components, which may possibly be representative

of different physical content. By removing irrelevant POD modes, it should be possible to extract essentially the pure travelling wave component corresponding to the short-wavelength elliptic instability within the signal. To this end, note that the first three POD modes can be associated with the mean base flow (M_1), and random meandering of the vortices (M_2 and M_3), similar to the decomposition for an isolated single vortex shown in the Appendix. Mode M_4 contains a combination of $m = 0$ and $|m| = 1$ azimuthal wavenumbers (unlike the case in the Appendix). This possibly accounts for fluctuations in the size of the vortex core and/or the distortion caused by the Crow instability. In any case, it contains negligible $|m| = 2$ azimuthal wavenumber content. It turns out that the next two highest amplitude modes, M_5 and M_6, show the correct characteristics required to reconstruct that part of the signal corresponding to elliptical instability. Those two POD modes are presented in figures 11(*b*) and 11(*c*). Clearly, both modes contain significant $|m| = 2$ azimuthal wavenumber content, which is quantified below. Note also that the azimuthal distributions are offset in phase by approximately 45°, which is required to reconstruct a spatio-temporally varying helical mode.

To analyse precisely the azimuthal dependence of each POD mode, a Fourier decomposition was used in the azimuthal direction for each radial position r. For each value of the wavenumber $|m|$, we obtain the Fourier coefficients as functions of r. The results of these computations are shown in figure 13. In figure 13(*a*), since no other branch reaches the order of magnitude of the branch $|m| = 2$, M_5 can be considered as a pure spatial wave with an azimuthal wavenumber $|m| = 2$. Similarly, figure 13(*b*) shows two dominant branches at the highest order, revealing the coupling of two spatial waves of azimuthal wavenumbers $m = 0$ and $|m| = 2$. Note that M_6 can therefore be considered as the superposition of two azimuthal waves. The presence of the $m = 0$ component is revealed in figure 11(*c*) by the amplitude at the centre that does not fall to zero. As discussed above, the elliptic instability essentially relies on the interaction of Kelvin modes with azimuthal wavenumbers differing by 2. We can write

$$M_5 = \hat{A}(r)\sin(2\theta + \phi_0), \qquad (3.12a)$$

$$\tilde{M}_6 = M_6 - \hat{C}(r) = \hat{B}(r)\sin(2\theta + \phi_0 + 2\phi), \qquad (3.12b)$$

where $\hat{A}$, $\hat{B}$ and $\hat{C}$ are radial functions and ϕ is the phase difference between M_5 and $\tilde{M}_6$, the $|m| = 2$ component of M_6.

We can show that a travelling wave $Y = \hat{Y}\sin(2\theta + \omega_f t)$ expressed in the (M_5, M_6) basis must read

$$Y = \frac{\hat{Y}}{\hat{A}}\frac{\sin(-\phi_0 - \phi + \pi + \omega_f t)}{\sin(\phi)}M_5 + \frac{\hat{Y}}{\hat{B}}\frac{\sin(-\phi_0 + \omega t)}{\sin(\phi)}\tilde{M}_6. \qquad (3.13)$$

In (3.13), the factors of M_5 and $\tilde{M}_6$ are the coordinates of Y. Experimentally, it is possible to extract the projection X_5 and X_6 of the frames on M_5 and M_6. This is illustrated in figure 14, for about 0.1 s. Over this time interval, X_5 and X_6 are almost periodic, with a constant phase difference χ, a similar amplitude $\hat{X}$ and a zero mean value. They can be approximately modelled by

$$X_5 = \hat{X}(r)\sin(\omega_f t + \chi_0) \qquad (3.14a)$$

and

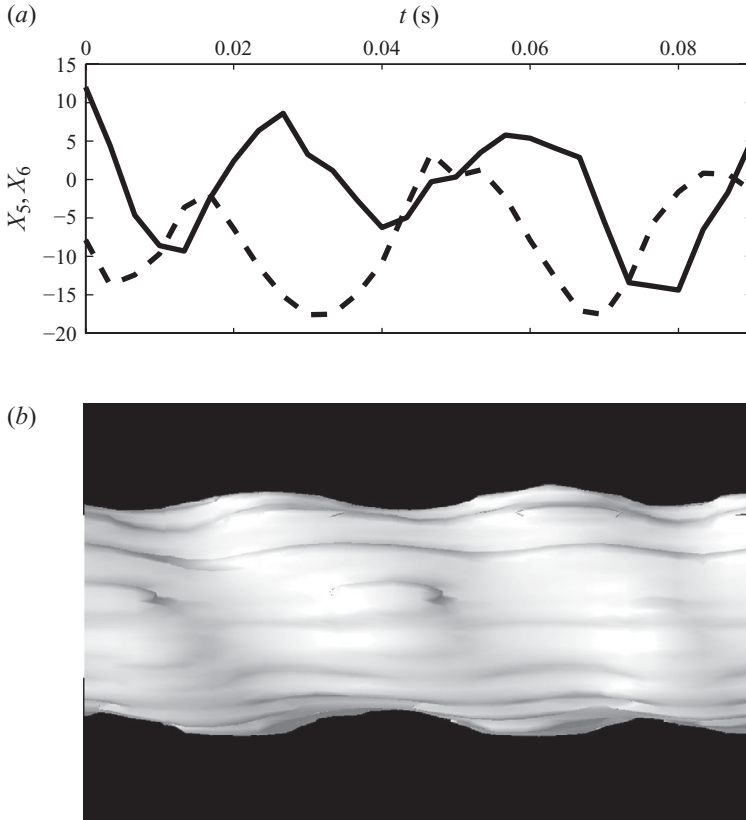$$X_6 = \hat{X}(r)\sin(\omega_f t + \chi + \chi_0). \qquad (3.14b)$$

FIGURE 14. (*a*) Projection of the frames on modes 5 (solid line) and 6 (dashed line). (*b*) Spatio-temporal reconstitution of the initial field using only the components of modes 1, 5 and 6. One field corresponds to one instant, and the spatio-temporal field is reconstituted by placing side by side the two-dimensional fields.

According to (3.13), if X_5 and X_6 are to be associated with the coordinates of a travelling wave in the $(M_5, \tilde{M}_6)$ space, their relative phase difference must be such that $\chi = \phi \pm \pi$. Experimentally, we can measure the angular phase difference $\tilde{\phi}$ between M_5 and M_6 by a cross-correlation. We find $\tilde{\phi} = 45.0°$ so $\phi = 2\tilde{\phi} = 0.50\pi$. By measuring the temporal shift τ of X_6 relative to X_5, and their period T, we obtain $\chi = 2\pi\tau/T = 0.58\pi$. Given the uncertainty in the measurement of τ due to the low temporal resolution of X_5, we can conclude that X_5 and X_6 are good candidates to be the coordinates in $(M_5, \tilde{M}_6)$ of a spatio-temporal travelling wave. This is illustrated and confirmed by figure 14(*b*). It shows the spatio-temporal reconstruction of the field formed by placing side by side the successive projections of the frames on the modes 1, 5 and 6. Mode 1 can be considered as the mean field, found by averaging the light intensity of all the frames. Figure 14(*b*) shows a double-helix structure, typical of a second-order azimuthal symmetry wave. The $m = 0$ component of M_6 just adds a periodic axisymmetric deformation to the helix, hardly visible in figure 14(*b*). Using the correspondence between the vorticity and the light intensity of the frames demonstrated in the Appendix, we can extend these conclusions to the vorticity field. A physical interpretation can be made by considering the perturbation field of the total field, presented in figure 14(*b*), as the superposition of two Kelvin modes of pulsation frequency ω_f and with different azimuthal wavenumbers $m = 0$ and $|m| = 2$.
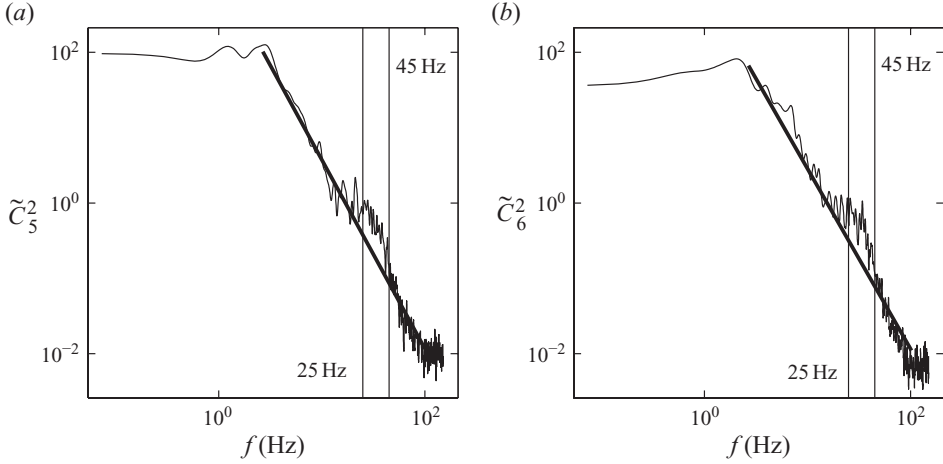
FIGURE 15. (*a*) Power spectral density P_5 of the coordinates of all the frames of mode 5. The solid line represents the average slope of P_5. The two vertical lines delimit a zone in which the distance between P_5 and the line of average slope is maximal. (*b*) Same as (*a*) for mode 6.

We now wish to make a link between these conclusions and the elliptic instability theory. The first step is to measure ω_f more accurately. To do so, a Fourier analysis of the coordinates, in (M_5, M_6), of all the frames acquired, is performed. The corresponding power spectral densities P_5 and P_6 are plotted in figure 15. A low-frequency peak can clearly be seen for P_5 and P_6. This is due to the Crow instability, coupled with the meandering phenomenon. These two mechanisms impose a translation of the vortex that can be modelled by an $m = 1$ perturbation, but their high energetic levels also contaminate the more complex modes. A frequency range of more interest is found between 25 and 45 Hz. As can be seen in figure 15, it corresponds to the zone where the distance between P_5 and the linear approximation of P_5 in the middle range frequency is maximal. The same applies to P_6. This gives the approximation $\omega_f/2\pi = (35 \pm 10)$ Hz. Non-dimensionalising by $2\pi b^2/\Gamma_1$, we find

$$90 < \omega_f^* < 160. \qquad (3.15)$$

The non-dimensional apparent pulsation of a spatial double helix of wavelength λ_1, translating without rotation along its axis at a velocity U_1 with respect to a fixed observer, is equal to 135. This is the same order of magnitude as ω_f^*, which means that the observed pulsation is mainly due to the translation of a spatial pattern through a fixed observation plane. This is consistent with the fact that the numerically obtained value of the pulsation (in the frame or reference of the helix) is an order of magnitude smaller. The spatio-temporal reconstruction, presented in figure 14, can therefore be interpreted as almost purely spatial, by making the transformation $z \to -U_\infty t$. Since λ_1 is positive, we can then conclude on the positive sign of m by inspecting the angular velocity phase of the wave. The equivalent axial wavelength λ_f reads

$$\lambda_f = 2\pi U_{\infty 1}/\omega_f = 1.57\,\text{cm}, \qquad (3.16)$$

which is very close (within 2 %) to the measured value $\lambda_1 = 1.60\,\text{cm}$.

We conclude that the results and analysis are consistent with the identification of the elliptic instability in the present flow. To reiterate, we identified a periodic unstable perturbation, decomposed this perturbation and showed that it was the result of the coupling of a spatial wave of azimuthal wavenumber $|m| = 2$ with an
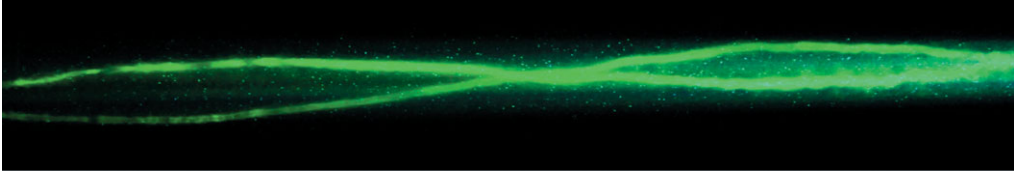
FIGURE 16. (Colour online) Side view of the co-rotating vortex pair. The field of view is approximately 8 cm × 50 cm.

$m = 0$ (axisymmetric) wave. The difference between the two wavenumbers is equal to 2, which is typical of the elliptic instability (see (3.8)). Despite a difference in the axial wavelength, the structure of the unstable mode, as well as the growth rate, is consistent with that of the most unstable mode obtained numerically by analysing the stability of the experimental base flow.

4. Co-rotating vortex pair

In this section, we investigate the stability of a co-rotating vortex pair with axial core flow. Such pairs were generated in the water channel by changing the sign of the angle of attack of one of the wings, with respect to the configuration used in the previous section. The values of free-stream velocity and angles of attack, as well as the relative position of the two aerofoils, were varied until a short-wavelength perturbation could be observed on the vortices. One such configuration was then selected for a more detailed analysis. It consisted of the two wings being offset in the horizontal direction (x), with the tips of their trailing edges located at the same vertical position (y). The angle of attack was 8° for both wings, and the tips were separated by 2.5 cm in the x-direction. The free-stream velocity was approximately 65 cm s^{-1}, resulting in a chord-based Reynolds number of about $Re_{chord} = 70\,000$.

4.1. *Characteristics of the three-dimensional base flow*

Figure 16 shows a side view of a dye visualisation of the co-rotating vortex pair. Mutual induction of the two vortices results in a rotation of the pair as it moves downstream (towards the right) in the channel, which produces the double-helix configuration visible in this figure.

Following the procedure described for the counter-rotating pair, 300 velocity fields were measured at $z/c = 9.0$, using stereo-PIV. This downstream position was chosen for analysis even though the elliptic instability had already started to develop because the base flow takes longer to fully develop with the wing set-up for corrotating vortices. The same recentring method was used to remove the effect of the vortex motion on the time-averaged velocity fields. Figure 17 shows a reconstruction of the total mean field. For negative values of x (to the left of the middle plane), the fields were recentred relatively to the top vortex and then averaged. The same procedure was applied to the bottom vortex to compute the rest of the field. Considering one vortex, the stretching direction of the average vorticity distribution follows approximately the principal direction of the strain field induced by the other vortex. For the axial velocity distribution, the stretching direction is governed by the main part of the wake of the wing, which spirals around the vortices. For each vortex, the total circulation was estimated by integrating the velocity field on a closed rectangular contour surrounding the vortex, as for the counter-rotating case. The vortices were found to be, to a good approximation, equal in strength.
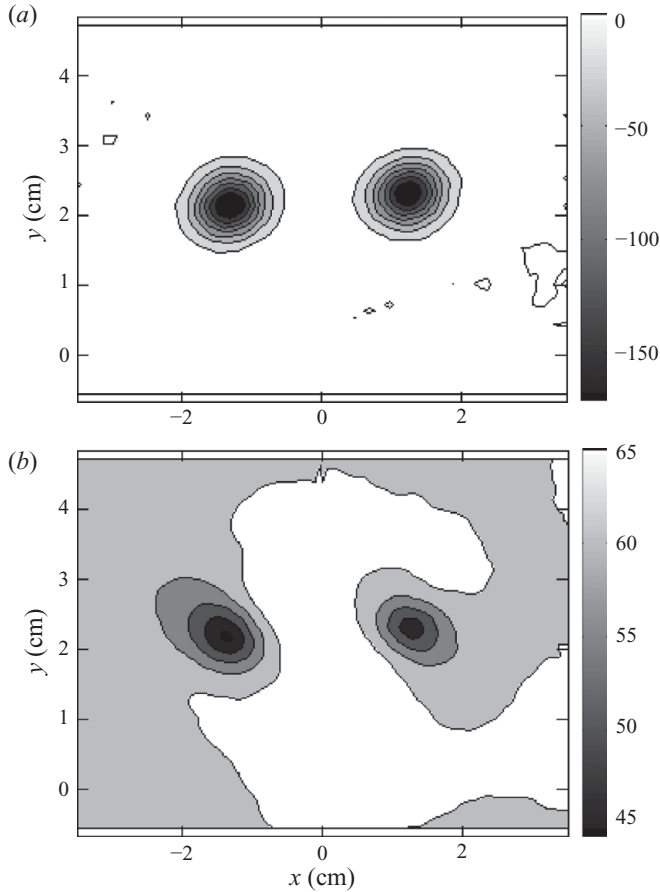
FIGURE 17. Reconstructed time-averaged vorticity (*a*) and axial velocity (*b*) fields at $z/c = 9.0$. The top vortex is now on the left.

In the attempt to model the azimuthally averaged azimuthal velocity profile U_θ, contrary to the counter-rotating case, Gaussian functional fits did not lead to acceptable results. Instead, following the approach of Fabre & Jacquin (2004), the measured profile U_θ was fitted to their VM2 vortex model. The match is excellent, as shown in figure 18(*a*), which also shows the Gaussian fit for comparison. The failure of the Gaussian model to provide an acceptable fit in this case is probably due to the wing sections being set at opposing angles, which leads to more interference between the flows over each wing with a consequent significant downstream effect. The parameters obtained for each vortex are listed in table 3. The two vortices are very similar. As for the counter-rotating case, U_∞ is defined as the value of the axial velocity profile at $r/\rho_1 = 3$. The non-dimensional parameter W_0 in this case is equal to $W_0 = (U_0 - U_\infty)2\pi\rho_1/\Gamma$. Here W was very well fitted by a Gaussian function (see figure 18), and W_{01} is observed to be 12 % greater than W_{02}. This difference is mainly due to a higher axial velocity defect in the centre of the top vortex compared to the bottom vortex, since the top wing is longer than the bottom wing.

In order to characterise the evolution of the vortex positions with downstream distance z, a laser sheet oriented in a direction normal to the free stream was placed at $z/c = 1.7, 4.8, 7, 8.8$ and 9.8. Dye was injected at both wing tips. For each streamwise

		Top vortex		Bottom vortex
Γ	$cm^2\,s^{-1}$	-169		-170
ρ_1	cm	0.45		0.44
ρ_2	cm	2.14		2.30
ϕ		0.62		0.59
a_W	cm	0.47		0.46
b	cm		2.69	
Γ/ν		18 000		18 100
ρ_1/b		0.17		0.16
a_w/ρ_1		1.04		1.05
W_0		0.33		0.29

TABLE 3. Parameters of the base flow extracted from stereo-PIV measurements for co-rotating vortices. The azimuthally averaged azimuthal velocity profile was fitted with a VM2 model defined by (2.2). Indices 1 and 2 refer to the upper and lower vortices, respectively.
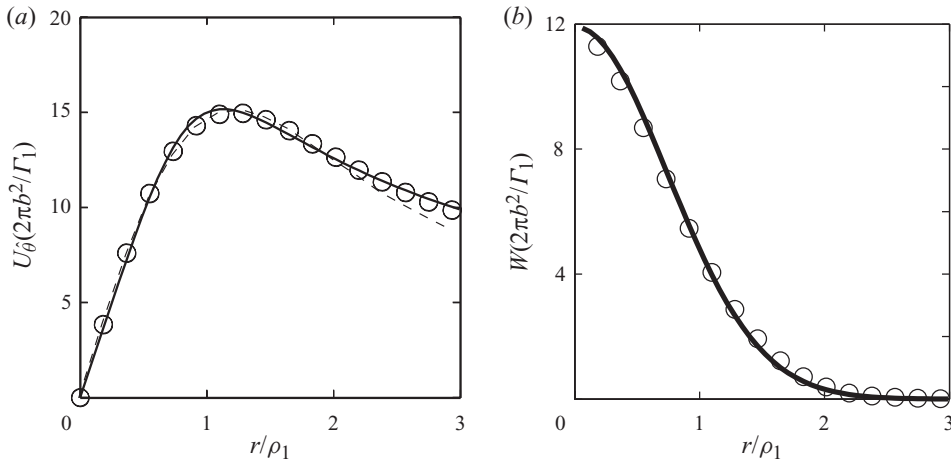

FIGURE 18. (*a*) Azimuthally averaged azimuthal velocity profile for the top vortex $U_{\theta 1}$, as a function of the radius r. The experimental points are symbolised by dots. The solid line corresponds to the VM2 model. The fit to a Gaussian model is shown by the dashed line. (*b*) Same as (*a*) for the axial velocity defect W_1 fitted to a Gaussian function.

location, 6000 frames showing vortices were acquired. For every frame, each vortex was localised by computing the 'centre of mass' of the light intensity. Averaging the coordinates obtained for each z/c gives a reliable estimation of the vortex positions in the (x, y)-plane. This is illustrated in figure 19. It is clear that the vortex pair moves upwards as z/c increases. A possible explanation for this behaviour could lie in the large-scale background flow (rotation), induced by the wings inside the test section, which may entrain the vortex system away from its initial x–y position.

The separation distance b evolved approximately linearly with z/c, varying from $b = 4.2$ cm at $z/c = 4.8$, to $b = 2.4$ cm at $z/c = 9.8$. A similar linear evolution was observed for the angle ϑ between the line joining the average position of the vortices and the x-axis, as shown in figure 20. This is a sign that the merging process has not yet begun (Meunier & Leweke 2005). Note that the predicted vortex co-rotation rate based on the vortex circulations matches the observed rate to within a few per cents.
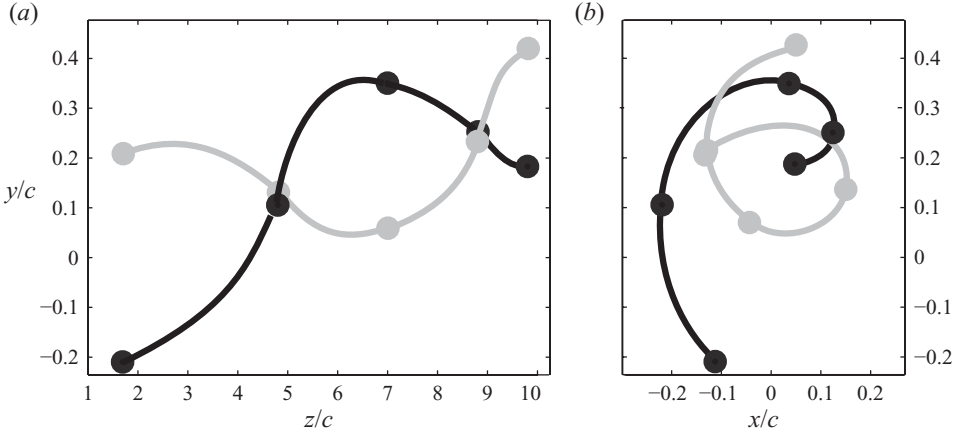
(a)

(b)

FIGURE 19. Position of the vortices in the (z, y) plane (a) and (x, y) plane (b). Note that the scales of x- and y-axes are the same but different from the z-axis scale.
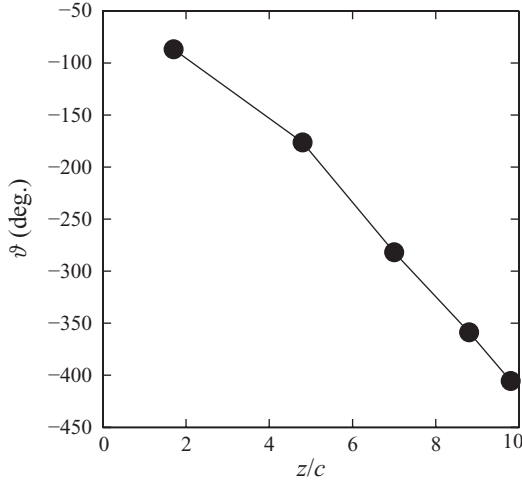
FIGURE 20. Angle ϑ formed by the wing-tip axis and the line linking the average position of the vortices, as a function of the streamwise position z/c.

4.2. Elliptic instability

Following the procedure used for the counter-rotating pair, fluorescein dye was injected into the top vortex, allowing it to be illuminated in volume in a direction parallel to the free stream. At $z/c = 9.5$, 200 frames of the top vortex were captured. Of these, 15 exhibited a short-wave perturbation with an observable axial wavelength λ; an example is shown in figure 21. Averaging the measured values, we find

$$\lambda_1 = (1.09 \pm 0.12) \text{ cm}, \tag{4.1}$$

which corresponds to the non-dimensional axial wavenumber

$$k\rho_1 = 2\pi\rho_1/\lambda_1 = 2.59 \pm 0.36. \tag{4.2}$$

The perturbation is symmetric with respect to the axis of the vortex. This indicates an even order of azimuthal symmetry. Since it is not visible upstream of $z/c \approx 9$, this perturbation is unstable and presumably triggered by the flow.
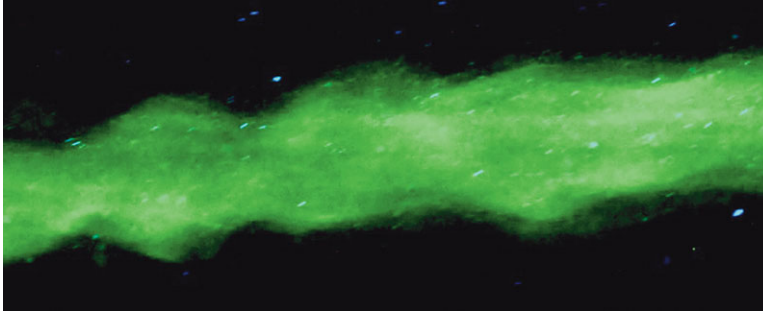
FIGURE 21. (Colour online) Visualisation of the instability propagating on the top vortex at $z/c = 9.5$. The field of view is approximately $2\,\mathrm{cm} \times 5\,\mathrm{cm}$.
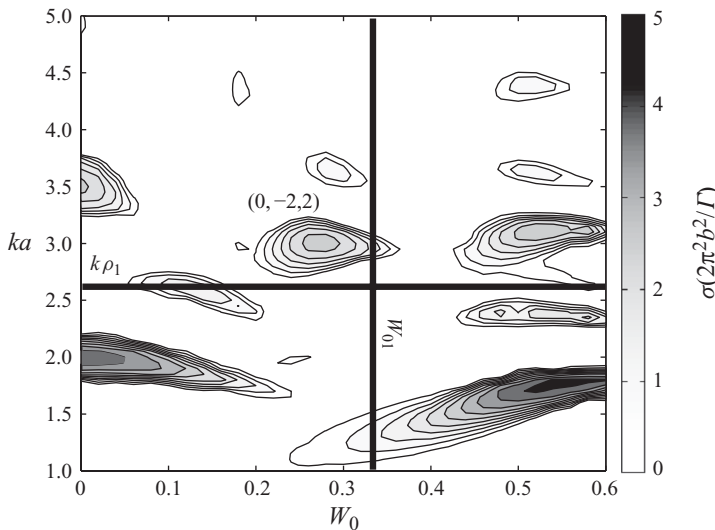

FIGURE 22. Contours of instability growth rate in the (W_0, ka) plane for $a/b = 0.14$ and $\Gamma/\nu = 14\,000$ (from Roy *et al.* 2008). The thick lines represent the conditions of the present experiment.

The theory of the elliptic instability, presented in § 3.3.1 for counter-rotating vortices (stationary strain field), also applies to co-rotating vortices. The rotation of the mutually induced strain field at the rate Ω changes the resonance condition (3.8) to

$$\begin{pmatrix} k_1 \\ m_1 \\ w_1 \end{pmatrix} - \begin{pmatrix} k_2 \\ m_2 \\ w_2 \end{pmatrix} = \begin{pmatrix} 0 \\ \pm 2 \\ \pm \Omega \end{pmatrix}. \tag{4.3}$$

Here Ω is the co-rotation rate of the vortex pair. From this condition, if the growing perturbation is caused by the elliptic instability mechanism, it would necessarily be the result of a resonance between Kelvin modes with $m_1 = 0$ and $|m_2| = 2$ or $|m_1| = 2$ and $|m_2| = 4$. Higher-order mode combinations are unlikely to be visible experimentally since local minima will be partially hidden by maxima shifted by an angle of $\pi/4$ in the azimuthal direction. Figure 22 qualitatively compares the wavelength obtained

in the experiment to the numerical results of Roy *et al.* (2008), who studied the elliptic instability in a pair of Gaussian co-rotating vortices with axial flow. The experimental point is close to the instability island of the $(0, -2, 2)$ mode. For the value of W_0 measured experimentally, this mode is the most unstable one. The spatial structure of this mode is consistent with our observations. Given the fact that the base flow analysed is different in the two studies, the comparison remains qualitative, but it suggests that the $(0, -2, 2)$ mode is likely to be the cause of the observed instability. Note that the contour plot corresponds to $a/b = 0.14$ and a circulation-based Reynolds number of $\Gamma/\nu = 14\,000$, while the values for the co-rotating pair are $\rho_1/b = 0.17$ and $\Gamma/\nu = 18\,000$. However, the positions of the instability islands are not strongly affected by either the vortex separation or the Reynolds number. Of interest is that the equivalent core size, a, based on a Gaussian model fit is at least 10 % larger than the VM2 model fit for ρ_1 (see figure 18a). This means that the equivalent ka of the experimental conditions in terms of the Gaussian model is approximately 3, i.e. lying close to the vertical position of the $(0, -2, 2)$ instability island of the figure.

5. Conclusions

In this paper, we have presented experimental results concerning the short-wavelength elliptic instability of a pair of co- and counter-rotating vortices with an axial velocity inside the core. This instability was previously observed clearly only in vortex pairs without axial flow (Leweke & Williamson 1998; Meunier & Leweke 2005). It is demonstrated here to persist with the addition of axial velocity. Dye visualisations and stereoscopic PIV measurements have given qualitative and quantitative information on the spatial structure of the observed instability mode.

The axial wavelength of the short-wave instability was determined experimentally from dye visualisations of the vortex pairs. For the counter-rotating case, it was found to be in good agreement with predictions from a linear stability analysis performed numerically on the experimental base flow. Part of the discrepancy may be due to the difficulty in defining the base flow responsible for the wavelength selection. The instability is observable at a given downstream position, where its amplitude is high enough to be detectable, but it was also growing on the vortex at upstream positions. The exact location where it was initiated, i.e. where the wavelength is selected, is difficult to determine.

For the counter-rotating case, the experimental growth rate of the instability was determined from measurements of the amplitude at different downstream locations. The result matches very well with the numerical growth rate of the most unstable mode from elliptic instability theory.

A POD based on dye visualisation of the top vortex was carried out, in order to investigate in detail the spatial structure of the observed unstable mode. It revealed a superposition of two three-dimensional waves of similar magnitude, which can be related to Kelvin modes, both periodic in the axial direction. The first wave is axisymmetric, corresponding to an azimuthal wavenumber $m = 0$; the second wave has a second-order azimuthal symmetry ($m = 2$). The difference of 2 in the azimuthal wavenumber is typical of an elliptic instability of a vortex pair. Moreover, the azimuthal symmetry of the two waves corresponds exactly to the azimuthal symmetry of the two Kelvin modes resonating to form the most unstable mode obtained from numerical stability analysis.

In summary, in this study we have presented clear evidence of a short-wavelength three-dimensional instability, developing in counter- and co-rotating vortex pairs with

cU_∞/ν	Γ/ν	ρ_2/ρ_1	γ	a_w/ρ_1	W_0
46 600	8700	5.52	0.48	1.31	0.27

TABLE 4. Parameters of the base flow extracted from the stereo-PIV measurements.

axial core flow. The spatial structure of the unstable perturbation is characterised by an azimuthal wavenumber $m = 2$, resulting in a double-helix structure of the perturbed vortex core. This is different from the short-wave instability modes previously observed on vortex pairs without axial flow, which have an azimuthal variation with $m = \pm 1$. Qualitative and quantitative comparison of the experimental results with theoretical/numerical stability analysis has clearly identified this phenomenon as an elliptic instability of the vortex cores, caused by the mutually induced strain of the vortices.

Appendix. Relation between vorticity and dye POD modes

We here demonstrate that the modes extracted by POD (Berkooz *et al.* 1993; Chatterjee 2000; Liang *et al.* 2002) on the vorticity field of a single vortex show the same basic characteristics of the modes as extracted by POD based on the light intensity of image frames where the vortex is visualised by fluorescent dye.

For this work, presented in Roy & Leweke (2008), the same set-up as described in § 2 was used. However, in this case only the bottom wing was used to generate a single tip vortex in the free stream. The angle of attack was fixed at 6° and the free-stream velocity set to 46.6 cm s^{-1}. A total of 400 stereo-PIV measurements were taken to extract the three components of the velocity in a plane normal to the free stream at $z/c = 11.2$. Following the recentring method presented in § 3.1, the axisymmetric azimuthal velocity profile U_θ was fitted by the two-scale vortex model, VM2 defined by (2.2). The match is excellent. The axial velocity defect profile was fitted to a Gaussian function. The flow was characterised by the non-dimensional parameters listed in table 4.

The best way to accurately compare the results of the POD analysis on the vorticity and the light intensity is to run the POD on the same instantaneous flow images for the two procedures. To make this possible, in addition to the Dantec particles used previously for the stereo-PIV measurements, some fluorescein was injected at the wing tip and advected with flow. At $z/c = 11.2$, an argon ion continuous laser illuminated the flow in a vertical plane normal to the free stream. A cylindrical lens was used to focus the laser power on a small zone containing the vortex. A high-speed video camera was positionned at the end of the test section, capturing the laser plane through the visualisation window presented in figure 1. In all, 16 000 images were recorded at an acquisition rate of 2000 Hz. This rate was determined from the constraints on the time separation of images for PIV. On each frame, the particles seeding the flow and a dye patch similar to that presented in figure 11 were visible. The light intensity level reflected by the particles was higher than the dye patch, allowing the measure of the two component velocity field using planar PIV. For each frame, the vorticity was computed. The POD procedure based on singular value decomposition described in § 3.3.2 was followed to extract the set of optimal
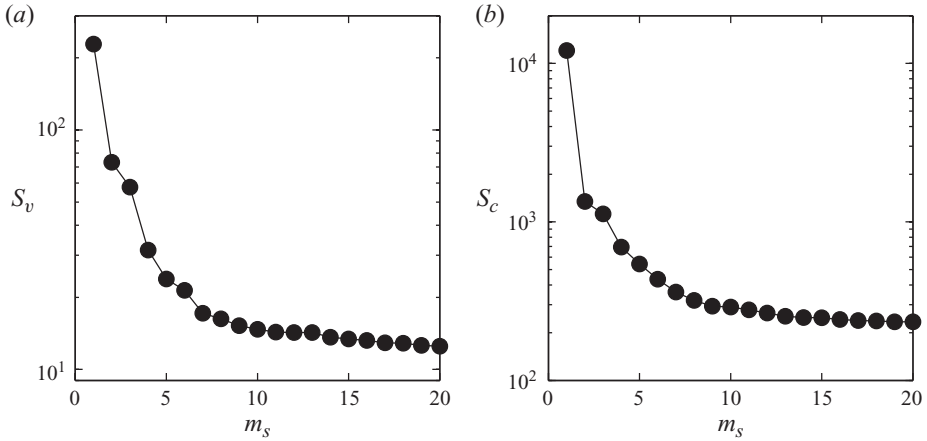
FIGURE 23. Comparison of the distributions of the first 20 singular values computed from the (a) vorticity fields (S_v) and (b) the dye intensity (S_c).
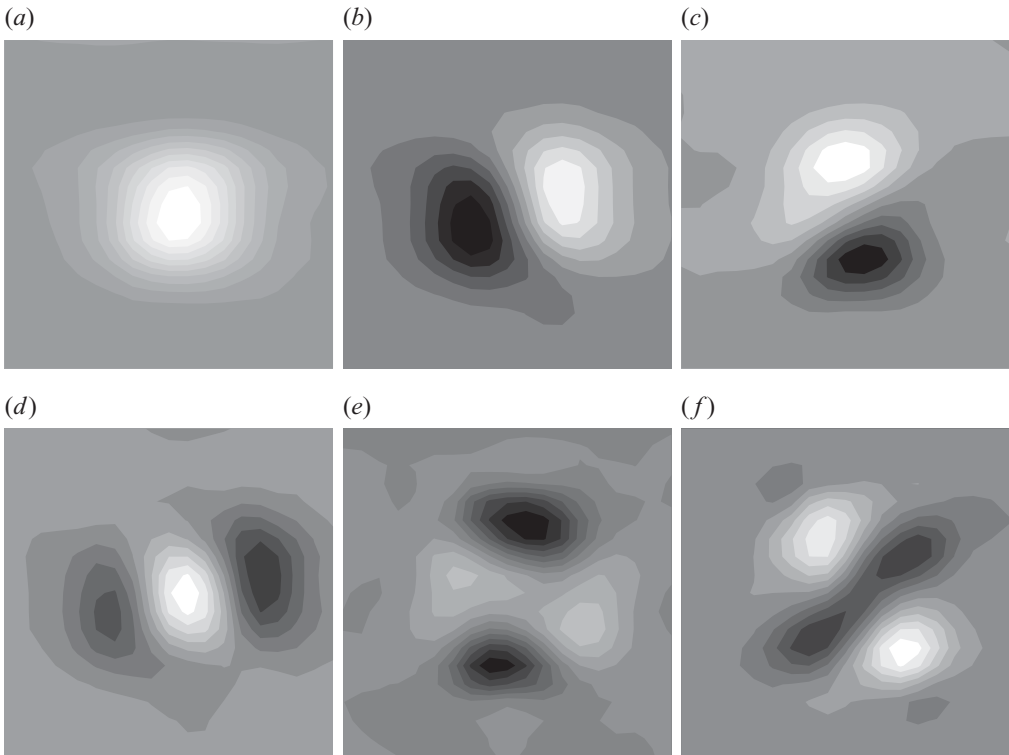

FIGURE 24. Modes computed by singular value decomposition of the vorticity field time series obtained by high-speed PIV for a single vortex ($Re = 8700$ and $W_0 = 0.27$). (a–f) The six most energetic modes are shown.

modes for the vorticity and the light intensity. The singular values are presented in figure 23. The corresponding modes can be found in figures 24 and 25. The dimensions of the zone plotted in all the modes presented in figures 24 and 25, and the scale of the axes, are the same. Also, the colour scale is symmetric with respect to 0,
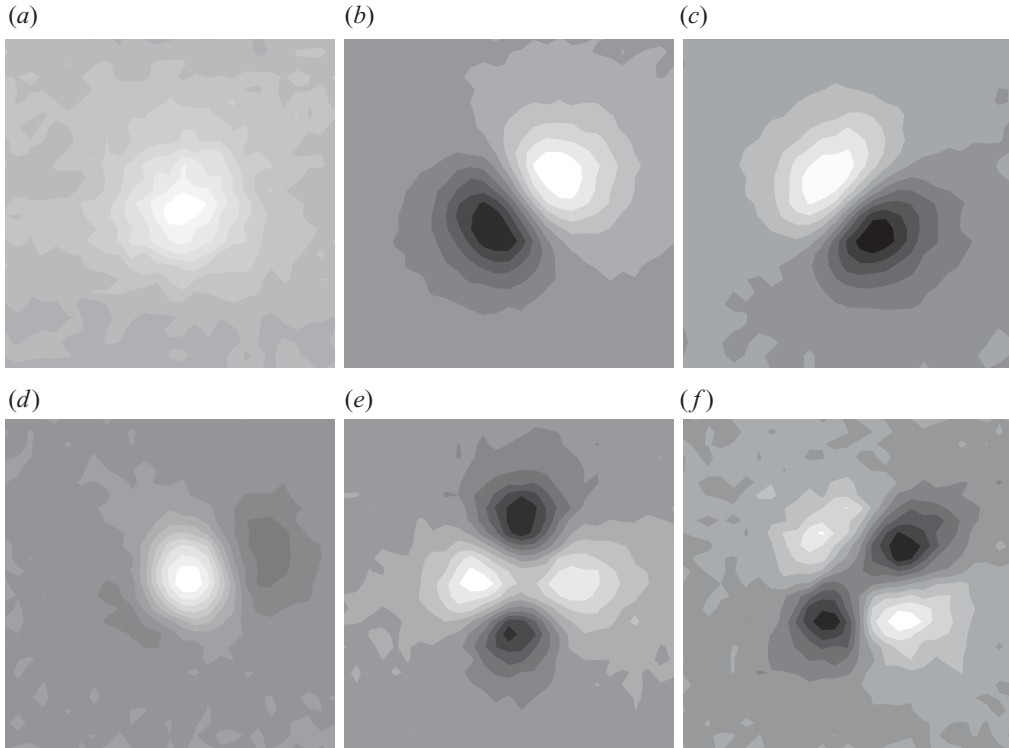
FIGURE 25. Same as figure 24, but obtained from dye intensity time series.

from black to white. Figures 23(*a*) and 23(*b*) look qualitatively alike. The singular values, which can be seen as the energy of the corresponding singular vector, rapidly decrease with the increasing order. The first mode corresponds to the mean field. In both cases, they show an axisymmetric zone (to the first order) around which the relative magnitude always has the same sign. The energy of this mode is much higher than the others. Modes 2 and 3 are, in both cases, associated with a global displacement of the vortex in the plane. They can be seen as a pure azimuthal wave of wavenumber $m = 1$. The only difference that can be noticed is a small tilt of the dye modes compared to the vorticity modes. This can be explained by the fact that the preferred direction of motion of the vortex is not very sharply defined as shown by Roy & Leweke (2008) for this flow. Nevertheless, the relative orientation of modes 2 and 3 remains constant at 90°. In figure 23, modes 2 and 3 form a doublet of similar energy, well separated from the rest of the modes. Both vorticity and dye POD identify the vortex displacement as the most energetic perturbation. Modes 4–6 also look very similar. They all seem to result from the combination of $m = 2$ and $m = 0$ waves. Their absolute and relative directions are similar. The vorticity modes 4–6 are slightly more isolated in the singular value hierarchy than the dye modes. They form a triplet that is easily visible in figure 23(*a*). Nevertheless, the rank of the modes is the same.

In conclusion, the match between vorticity and light intensity modes obtained by POD is excellent. The same spatial structures were revealed in both cases. Furthermore, the hierarchy in the energy levels is conserved. This leads to the conclusion that, in

our flow configuration, a POD analysis can be performed on dye visualisations to obtain information on the vorticity modes.

REFERENCES

ALKISLAR, M. B., KROTHAPALI, A. & LOURENCO, L. M. 2003 Structure of a screeching rectangular jet: a stereoscopic particle image velocimetry study. *J. Fluid Mech.* **489**, 121–154.

ANTKOWIAK, A. & BRANCHER, P. 2004 Transient energy growth for the Lamb–Oseen vortex. *Phys. Fluids* **16**, L1–L4.

ARENDT, S., FRITTS, D. C. & ANDREASSEN, Ø. 1997 The initial-value problem for Kelvin vortex waves. *J. Fluid Mech.* **344**, 181–212.

BAYLY, B. J. 1986 Three-dimensional instability of elliptical flow. *Phys. Rev. Lett.* **57**, 2160–2163.

BERKOOZ, G., HOLMES, P. & LUMLEY, J. L. 1993 The proper orthogonal decomposition in the analysis of turbulent flows. *Annu. Rev. Fluid Mech.* **25**, 539–575.

BILLANT, P., BRANCHER, P. & CHOMAZ, J.-M. 1999 Three-dimensional stability of a vortex pair. *Phys. Fluids* **11**, 2069–2077.

BOULANGER, N., MEUNIER, P. & LE DIZÈS, S. 2007 Structure of a tilted stratified vortex. *J. Fluid Mech.* **583**, 443–458.

BOULANGER, N., MEUNIER, P. & LE DIZÈS, S. 2008 Instability of a tilted vortex in stratified fluid. *J. Fluid Mech.* **596**, 1–20.

BRISTOL, R. L., ORTEGA, J. M., MARCUS, P. S. & SAVAŞ, Ö. 2004 On cooperative instabilities of parallel vortex pairs. *J. Fluid Mech.* **517**, 331–358.

CARLIER, J. & STANISLAS, M. 2005 Experimental study of eddy structures in a turbulent boundary layer using particle image velocimetry. *J. Fluid Mech.* **535**, 143–188.

CHATTERJEE, A. 2000 An introduction to the proper orthogonal decomposition. *Curr. Sci. India* **78**, 808–817.

CHEN, A. L., JACOB, J. D. & SAVAŞ, Ö. 1999 Dynamics of corotating vortex pairs in the wakes of flapped airfoils. *J. Fluid Mech.* **382**, 155–193.

CROUCH, J. D. & JACQUIN, L. 2005 Aircraft trailing vortices/ tourbillons de sillages d'avions. *C. R. Phys.* **6** (Special Issue), 393–565.

CROW, S. C. 1970 Stability theory for a pair of trailing vortices. *AIAA J.* **8**, 2172–2179.

DEVENPORT, W. J., RIFE, M. C., LIAPIS, S. I. & FOLLIN, G. J. 1996 The structure and development of a wing-tip vortex. *J. Fluid Mech.* **312**, 67–106.

DEVENPORT, W. J., VOGEL, C. M. & ZSOLDOS, J. S. 1999 Flow structure produced by the interaction and merger of a pair of co-rotating wing-tip vortices. *J. Fluid Mech.* **394**, 357–377.

DEVENPORT, W. J., ZSOLDOS, J. S. & VOGEL, C. M. 1997 The structure and development of a counter-rotating wing-tip vortex pair. *J. Fluid Mech.* **332**, 71–104.

ELOY, C. & LE DIZÈS, S. 2001 Stability of the Rankine vortex in a multipolar strain field. *Phys. Fluids* **13**, 660–676.

ELOY, C., LE GAL, P. & LE DIZÈS, S. 2000 Experimental study of the multipolar vortex instability. *Phys. Rev. Lett.* **85**, 145–166.

FABRE, D. 2002 Instabilités et instationnarités dans les tourbillons: application aux sillages d'avions. PhD thesis, ONERA/Université Paris VI.

FABRE, D., COSSU, C. & JACQUIN, L. 2000 Spatio-temporal development of the long and short-wave vortex-pair instabilities. *Phys. Fluids* **12**, 1247–1250.

FABRE, D. & JACQUIN, L. 2004 Short-wave cooperative instabilities in representative aircraft vortices. *Phys. Fluids* **16**, 1366–1378.

FONTANE, J., BRANCHER, P. & FABRE, D. 2008 Stochastic forcing of the Lamb–Oseen vortex. *J. Fluid Mech.* **613**, 233–254.

GERZ, T., HOLZÄPFEL, F. & DARRACQ, D. 2002 Commercial aircraft wake vortices. *Prog. Aerosp. Sci.* **38**, 181–208.

HOERNER, S. F. 1965 *Fluid Dynamic Drag*. Hoerner Fluid Dynamics.

JACOB, J. D. 1995 Experimental investigation of the trailing vortex wake of rectangular airfoils. PhD thesis, University of California at Berkeley.

JIMÉNEZ, J. 1975 Stability of a pair of co-rotating vortices. *Phys. Fluids* **18** (11), 1580–1581.

KELVIN, LORD 1880 Vibrations of a columnar vortex. *Phil. Mag.* **10**, 155–168.

KERSWELL, R. R. 2002 Elliptical instability. *Annu. Rev. Fluid Mech.* **34**, 83–113.

KLEIN, R. & KNIO, O. M. 1995 Asymptotic vorticity structure and numerical simulation of slender vortex filaments. *J. Fluid Mech.* **284**, 275–321.

KLEIN, R., MAJDA, A. J. & DAMODARAN, K. 1995 Simplified equations for the interaction of nearly parallel vortex filaments. *J. Fluid Mech.* **288**, 201–248.

KRUTZSCH, C.-H. 1939 Über eine experimentell beobachtete Erscheinung an Wirbelringen bei ihrer translatorischen Bewegung in wirklichen Flüssigkeiten. *Annu. Phys. Leipzig* **427**, 497–523.

LACAZE, L., BIRBAUD, A.-L. & LE DIZÈS, S. 2005 Elliptic instability in a Rankine vortex with axial flow. *Phys. Fluids* **17**, 017101.

LACAZE, L., LE GAL, P. & LE DIZÈS, S. 2004 Elliptical instability in a rotating spheroid. *J. Fluid Mech.* **505**, 1–22.

LACAZE, L., LE GAL, P. & LE DIZÈS, S. 2005 Elliptical instability of a flow in a rotating shell. *Phys. Earth Planet. Inter.* **151**, 194–205.

LACAZE, L., RYAN, K. & LE DIZÈS, S. 2007 Elliptic instability in a strained Batchelor vortex. *J. Fluid Mech.* **577**, 341–361.

LANDMAN, M. J. & SAFFMAN, P. G. 1987 The three-dimensional instability of strained vortices in a viscous fluid. *Phys. Fluids* **30**, 2339–2342.

LAPORTE, F. & CORJON, A. 2000 Direct numerical simulations of the elliptic instability of a vortex pair. *Phys. Fluids* **12**, 1016–1031.

LE DIZÈS, S. & LAPORTE, F. 2002 Theoretical predictions for the elliptic instability in a two-vortex flow. *J. Fluid Mech.* **471**, 169–201.

LE DIZÈS, S. & VERGA, A. 2002 Viscous interactions of two co-rotating vortices before merging. *J. Fluid Mech.* **467**, 389–410.

LEIBOVICH, S., BROWN, S. N. & PATEL, T. 1986 Bending waves on inviscid columnar vortices. *J. Fluid Mech.* **173**, 595–624.

LEWEKE, T. & WILLIAMSON, C. H. K. 1998 Cooperative elliptic instability of a vortex pair. *J. Fluid Mech.* **360**, 85–119.

LEWEKE, T. & WILLIAMSON, C. H. K. 2011 Experiments on long-wavelength instability and reconnection of a vortex pair. *Phys. Fluids* **23**, 024101.

LIANG, Y. C., LEE, H. P., LIM, S. P., LIN, W. Z., LEE, K. H. & WU, C. G. 2002 Proper orthogonal decomposition and its applications. Part 1. Theory. *J. Sound Vib.* **252**, 527–544.

LIU, H.-T. 1992 Effects of ambient turbulence on the decay of a trailing vortex wake. *J. Aircraft* **29**, 255–263.

MALKUS, W. V. R. 1989 An experimental study of global instabilities due to tidal (elliptical) distortion of a rotating elastic cylinder. *Geophys. Astrophys. Fluid Dyn.* **48**, 123–134.

MAXWORTHY, T. 1972 The structure and stability of vortex rings. *J. Fluid Mech.* **51**, 15–32.

MEUNIER, P. & LEWEKE, T. 2001 Three-dimensional instability during vortex merging. *Phys. Fluids* **13**, 2747–2750.

MEUNIER, P. & LEWEKE, T. 2003 Analysis and optimization of the error caused by high velocity gradients in particle image velocimetry. *Exp. Fluids* **35**, 408–421.

MEUNIER, P. & LEWEKE, T. 2005 Elliptic instability of a co-rotating vortex pair. *J. Fluid Mech.* **533**, 125–159.

MOORE, D. W. & SAFFMAN, P. G. 1973 Axial flow in laminar trailing vortices. *Proc. R. Soc. Lond.* A **333**, 491–508.

MOORE, D. W. & SAFFMAN, P. G. 1975 The instability of a straight vortex filament in a strain field. *Proc. R. Soc. Lond.* A **346**, 413–425.

ORTEGA, J. M., BRISTOL, R. L. & SAVAŞ, Ö. 2003 Experimental study of the stability of unequal-strength counter-rotating vortex pairs. *J. Fluid Mech.* **474**, 35–84.

PIERREHUMBERT, R. T. 1986 Universal short-wave instability of two-dimensional eddies in an inviscid fluid. *Phys. Rev. Lett.* **57**, 2157–2160.

PRASAD, A. K. & JENSEN, K. 1995 Scheimpflug stereocamera for particle image velocimetry in liquid flows. *Appl. Optics* **34**, 7092–7099.

RENNICH, C. & LELE, S. K. 1997 Numerical method for incompressible vortical flows with two unbounded directions. *J. Comp. Phys.* **137**, 101–129.

ROSSOW, V. J. 1999 Lift-generated vortex of subsonic transport aircraft. *Prog. Aerosp. Sci.* **35**, 507–660.

ROY, C. & LEWEKE, T. 2008 Experiments on vortex meandering. European project 'FAR-Wake' (AST4-CT-2005-012238), *Tech. Rep.* TR 1.1.1-4. Available at: http://www.far-wake.org/.

ROY, C., SCHAEFFER, N., LE DIZÈS, S. & THOMPSON, M. C. 2008 Stability of a pair of co-rotating vortices with axial flow. *Phys. Fluids* **20**, 094101.

SARPKAYA, T. 1983 Trailing vortices in homogeneous and density-stratified media. *J. Fluid Mech.* **136**, 85–109.

SCHEIMPFLUG, T. 1904 Improved method and apparatus for the systematic alteration or distortion of plane pictures and images by means of lenses and mirrors for photography and for other purposes. *Great Britain Patent no. 1196*.

SCORER, R. S. & DAVENPORT, L. J. 1970 Contrails and aircraft downwash. *J. Fluid Mech.* **43**, 451–464.

SIPP, D. & JACQUIN, L. 2003 Widnall instabilities in vortex pairs. *Phys. Fluids* **15**, 1861–1874.

SPALART, P. R. 1998 Airplane trailing vortices. *Annu. Rev. Fluid Mech.* **30**, 107–138.

TAYLOR, J. R. 1997 *An Introduction to Error Analysis: The Study of Uncertainties in Physical Measurements*. University Science Books.

THOMAS, P. J. & AUERBACH, D. 1994 The observation of the simultaneous development of a long- and a short-wave instability mode on a vortex pair. *J. Fluid Mech.* **265**, 289–302.

TOMBACH, I. 1973 Observations of atmospheric effects on vortex wake behavior. *J. Aircraft* **10**, 641–647.

TSAI, C.-Y. & WIDNALL, S. E. 1976 The stability of short waves on a straight vortex filament in a weak externally imposed strain field. *J. Fluid Mech.* **73**, 721–733.

WALEFFE, F. 1990 On the three-dimensional instability of strained vortices. *Phys. Fluids* A **2**, 76–80.

WIDNALL, S. E., BLISS, D. & TSAI, C.-Y. 1974 The instability of short waves on a vortex ring. *J. Fluid Mech.* **66** (1), 35–47.

WIDNALL, S. E., BLISS, D. B. & ZALAY, A. 1971 Theoretical and experimental study of the instability of a vortex pair. In *Aircraft Wake Turbulence and Its Detection* (ed. J. H. Olsen, A. Goldberg & M. Rogers), p. 305. Plenum.

WIDNALL, S. E. & SULLIVAN, J. P. 1973 On the stability of vortex ring. *Proc. R. Soc. Lond.* A **332**, 335–353.

WILLERT, C. 1997 Stereoscopic digital particle image velocimetry for application in wind tunnel flows. *Meas. Sci. Technol.* **8**, 1465–1479.

ZANG, W. & PRASAD, A. K. 1997 Performance evaluation of a Scheimpflug stereocamera for particle image velocimetry. *Appl. Optics* **36**, 8738–8744.